Applied Energy 260 (2020) 114326

Contents lists available at ScienceDirect

Applied Energy

journal homepage: www.elsevier.com/locate/apenergy

Investigation of V-shaped blade for the performance improvement of vertical axis wind turbines

Jie Su[a], Yaoran Chen[a], Zhaolong Han[a,c,*], Dai Zhou[a,b,c,**], Yan Bao[a], Yongsheng Zhao[a]

[a] School of Naval Architecture, Ocean and Civil Engineering, Shanghai Jiao Tong University, Shanghai 200240, People's Republic of China
[b] Key Laboratory of Hydrodynamics of Ministry of Education, Shanghai Jiao Tong University, Shanghai 200240, People's Republic of China
[c] State Key Laboratory of Ocean Engineering, Shanghai Jiao Tong University, Shanghai 200240, People's Republic of China

HIGHLIGHTS

- The V-shaped blade is implemented to improve the power performance of VAWT.
- The V-shaped blade is a kind of low drag blade that increases the lift-drag ratio.
- The mechanisms of dynamic stalling and flow structures are studied carefully.
- The V-shaped blade alleviates the damage caused by lateral loads to VAWT.

ARTICLE INFO

Keywords:
V-shaped blade
Vertical axis wind turbine
Flow structure
Aerodynamic performance
Optimization

ABSTRACT

The vertical axis wind turbine (VAWT) is regarded as an important device to utilize the renewable offshore wind energy to supplement the existing power systems. Hence, the demand for higher wind energy conversion makes the research focus on the blade optimization of wind turbines. This paper attempts to propose a novel VAWT structure with V-shaped blade to improve the power outputs at moderate tip speed ratios. The feasibility of the Reynolds-Averaged Navier-Stokes SST $k-\omega$ turbulence model applied on the VAWT was verified against available experiments at first. Then a comprehensive investigation on the aerodynamic performance of such V-shaped VAWT was carried out using the SST k-ω model. The results indicated that the maximum enhancement in power coefficient obtained in the optimal V-shaped blade was about 24.1%. In addition to the great improvement of the power efficiency, the V-shaped blade was proven to alleviate the damage caused by lateral loads to the wind turbine. Besides, the flow structures over the blade surface were studied to reveal the mechanism of dynamic stall with the reason of power increase explained. Moreover, it was found that the V-shaped blade could effectively suppress the flow separation and delay the dynamic stall in the middle of the blade, and the undesirable blade tip effect would not be more serious comparing to that of the conventional straight blade. It was finally concluded that the current work could be practically applied to the design and optimization of the VAWT blades.

1. Introduction

Since the reduction of greenhouse gases became the common goal of the world, renewable energy has been considered as an important way to generate electricity. The offshore wind resource is one of the most important sustainable and clean energy sources due to its abundant reserves and has been utilized for many years [1]. In the past several decades, the horizontal axis wind turbines (HAWTs) have played an important role in the wind energy conversion. In order to achieve a higher energy efficiency ratio, great efforts have been made on the improvement of wind turbines such as maximization of the power production, optimization of the wind farm, and minimization of the blade mass [2,3]. Compared with the traditional horizontal axis wind turbine, the vertical axis wind turbine (VAWT) has been proved to be potentially dominant in the offshore wind utilization due to its advantages in simpler structure, lower cost and large scale development

* Corresponding author at: School of Naval Architecture, Ocean and Civil Engineering, Shanghai Jiao Tong University, Shanghai 200240, People's Republic of China.
** Corresponding author at: School of Naval Architecture, Ocean and Civil Engineering, Shanghai Jiao Tong University, Shanghai 200240, People's Republic of China.
E-mail addresses: han.arkey@sjtu.edu.cn (Z. Han), zhoudai@sjtu.edu.cn (D. Zhou).

https://doi.org/10.1016/j.apenergy.2019.114326
Received 25 August 2019; Received in revised form 2 December 2019; Accepted 3 December 2019
Available online 23 December 2019

[4].

One primary concern with the VAWT is that the conversion efficiency of wind energy is relatively lower than that of the HAWT. This may be a result of the complexity of the flow around VAWTs as well as a comparatively minor quantity of researches they had received. Thus, in recent years, researchers have made in-depth study to obtain a comprehensive understanding of the complex aerodynamic characteristics of VAWTs under different environmental conditions [5–7]. Various methods and techniques have been employed on the aerodynamics of VAWTs, including the Double-Multiple Streamtube Model [8–10], Vortex Model [11,12], Cascade Model [13], and Computational Fluid Dynamics (CFD) simulation [14–16]. Among these methods, CFD simulation is considered as a high-fidelity method which can provide much insight into the complete flow field [17] while the others do simplify the wake interaction, tip vortex and dynamic stall effects [18]. Besides, both wind tunnel and field experiments [19–23] have also played an important role with respect to flow field modeling and physical interpretations. All these methods and techniques have been utilized to evaluate the effects of a series of geometric parameters, such as pitch angle [17,24], symmetry [25], airfoil profile [26,27], solidity [27], and rotor aspect ratio [28]. The aerodynamic performance under various operational conditions, including different tip speed ratios [29], Reynolds numbers [30], turbulence intensities [31,32], as well as unsteady [33], skewed or vertical wind conditions [34,35], have also been investigated.

In addition to the aforementioned researches, in response to the growing appeals for novel configurations and optimized designs of VAWT to improve its power performance, some new concepts of configurations and blade profiles have been proposed recently. Xu et al. [36] carried out an experimental and numerical investigation on a disc-shaped wind rotor for a small-scale wind turbine. The influences of tip speed ratio, pitch angle and opening angle were estimated and a higher power coefficient of the wind rotor was obtained. Pérez-Torró and Kim [37] investigated the stalled flow characteristics of a NACA0021 airfoil with a wavy leading edge using the Large-Eddy Simulation (LES) technique. The results indicated that the increased lift force and the decreased drag force were achieved by using the wavy leading edge instead of the straight leading edge. Afterwards, Wang and Zhuang [38] applied leading-edge serrations to a VAWT at low tip speed ratios for performance improvement. The power output results showed that the improved configuration did reduce the impact of dynamic stall effect and increase the positive torque generation. Arpino et al. [39] proposed a new Darrieus-style VAWT with three couples of blades for the rotor, each composed by a main and an auxiliary airfoil. The new configuration was proven to have higher power coefficient at the lower tip speed ratios compared with the classical straight-bladed VAWT, which was suitable for urban applications. Chong et al. [40] redesigned the VAWT and proposed a cross axis wind turbine comprising three vertical blades and six horizontal blades arranged in a cross axis orientation. The deflectors were used to guide the oncoming flow upward which would interact with the horizontal blades and improve the performance of wind turbines. Besides, considering the advantages of Darrieus and Savonius wind turbine, Liu et al. [41] proposed a hybrid VAWT in which an inner modified-Savonius rotor was utilized to improve the self-starting capability. Another hybrid wind turbine was designed by Govind [42] who integrated a vertical axis wind turbine into a horizontal axis wind turbine to improve the aerodynamic performance.

Furthermore, in order to improve performance of the wind turbine, the helical blade was employed into VAWT, which was originally proposed for hydrokinetic turbines by Gorlov [43]. Apart from the studies of such turbines operating under water [44,45], the aerodynamic performance of helical VAWT has been investigated by both experimental measurements and numerical simulations. Scheurich and Brown [46] compared the aerodynamic performance of three VAWTs with different configurations, including straight-bladed configuration, curved-bladed configuration and helically twisted configuration. The helical VAWT was shown to be more efficient than the straight-bladed VAWT at constant rotational speed in unsteady wind conditions. The helical wind turbine experienced lower power loss when blade curvature and helical twist were optimized which resulted in a lower gradient in the variation of the power coefficient versus tip speed ratio. Cheng et al. [47] compared the results of a two-dimensional study and a three-dimensional simulation of a helical VAWT using the LES and the Reynolds-Averaged Navier-Stokes (RANS) models. The results showed that the power output was mainly affected by the variation of angle of attack and blade-wake interaction. Recently, Marten et al. [48] conducted the aero-elastic simulation for a helical VAWT built in Italy, in which the aerodynamic predictions was performed with the lifting line free vortex wake model. And the results were validated against experimental data and a blade element momentum simulation.

In addition to the improvement on the configuration of VAWTs, Zamani et al. [49] proposed a J-shaped profile as the blade airfoil for a straight-bladed vertical axis wind turbine. By eliminating a fraction of pressure side of the airfoil, the self-starting performance was improved. Besides, Ismail and Vijayaraghavan [50] investigated the effects of semi-circular dimple and Gurney flap at the airfoil surface on the aerodynamics of a vertical axis wind turbine. The response surface approximation was utilized to maximize the average torque and the modified airfoil was found to improve the performance of the wind turbine. After that, Sobhani et al. [51] made further investigation of dimple effects on Darrieus vertical axis wind turbine. A series of dimple shapes with different diameters, profiles, and locations were studied to enhance the aerodynamic performance. The results showed that the average efficiency and the optimal performance were 25% and 18% improved when using the blade with a cavity.

While numerous efforts have been made to improve the performance of the VAWT in previous studies, there is still more space for the wind turbine configuration improvement. In addition, compared to the complicated modification of blade profiles or configurations which would cause high manufacturing cost, a simple blade structure needs to be developed for practical application. And it would just slightly increase the cost if the existing manufacturing process of traditional straight blade could be utilized to manufacture the new blade configuration. Furthermore, detailed characteristics of the unsteady aerodynamics and the stall events, as well as the flow structure around the blade, still require further investigation.

In the present study, a novel VAWT with V-shaped blade will be proposed to improve the performance of the conventional straight-bladed Darrieus VAWT. A series of high-fidelity three-dimensional CFD unsteady simulations were performed to evaluate the effects of different V-shaped blades on the aerodynamics at a moderate tip speed ratio. The wind turbine model and the schematic of the V-shaped blade were presented in Section 2, then the details of computational domain and solver settings were demonstrated. The study was carried out using the RANS SST (shear stress transport) $k-\omega$ model, and the validation of the numerical model was achieved by comparing power coefficients at different tip speed ratios and dynamic torque as a function of azimuthal angle with experiments as shown in Section 3. In Section 4, the aerodynamic characteristics and performance of the V-shaped blade VAWT were investigated with respect to power coefficient, tangential and normal forces, torque coefficient, and the flow field. Besides, a deep insight into the cross-flow structure along the blade span was given by comparing the phenomena occurred on the surfaces of straight blade and V-shaped blade. Moreover, the pressure distributions over the blade at the middle section, the 3/4 span section and blade tip were compared for different azimuthal positions. Futhermore, the characteristics of the turbine wake were investigated. Finally, several conclusions were derived from the research results in Section 5.

The contributions of this work can be summarized as follows: (1) In the present study, a series of V-shaped blades were constructed and implemented on the rotor to greatly improve the power performance of VAWT. It would provide a new way for the design of wind turbines,

which could also be exploited in structure optimization. (2) The previous studies mainly focused on how to increase the lift of blade, while the present study provides a kind of low drag blade which can also improve the lift-drag ratio. (3) In previous studies, the aerodynamic loads, including torque, thrust and normal force, were investigated for different configurations or airfoil profiles. However, only a few studies reported the findings about the lateral force on VAWT, and to our knowledge, few study has shown the capability in decreasing lateral force. In the current study, the results cast a new light on the reduction in the damage to the VAWT caused by lateral force which prolongs the service life of wind turbines. (4) The current study provides a comprehensive comparison between the dynamic loads on the V-shaped blade and that of the conventional straight blade. The complete description of force-time history provides a detailed insight into the change of aerodynamics. (5) The present study would add to the knowledge of stalling mechanism by investigating the flow structure around blade, which has rarely been performed in previous study. And the comparisons of flow structure and pressure distribution at different positions along the blade span surely help to identify which part contributes to the performance improvements.

2. Methodology

2.1. Wind turbine model

A typical three-bladed vertical axis wind turbine is shown in Fig. 1, and the detailed geometric parameters of the studied VAWT are provided in Table 1. An equal scale prototype of the straight-bladed VAWT was selected from Castelli et al.'s study [19]. The NACA 0021 airfoil is used to produce the rotor blades, and the struts and shaft are neglected to simplify the model.

The solidity σ of the VAWT is defined as:

$$\sigma = \frac{Nc}{D} \tag{1}$$

where N is the blade number, c is the chord length and D is the rotor diameter.

Fig. 2 shows the mechanical characteristics of the blade during one revolution. Assuming that the freestream velocity is the same in the downwind region as in the upwind region [52], which means the effect of flow induction is not considered in the current study. Therefore, the relative local velocity W can be written as:

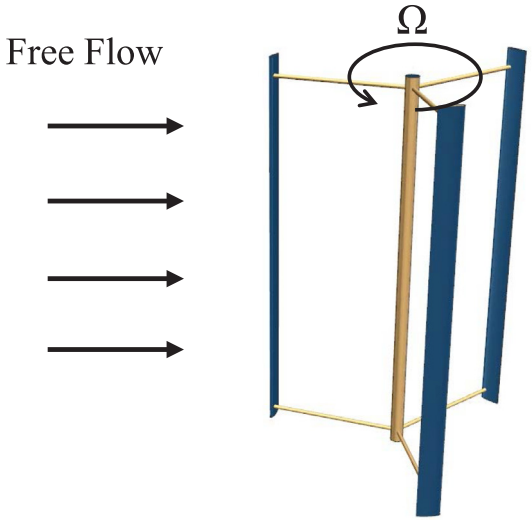

Fig. 1. The structure of a typical three-bladed vertical axis wind turbine.

Table 1
Geometric properties of the VAWT model [19].

Property	Symbol	Value
Airfoil profile	–	NACA 0021
Blade number	N	3
Chord length	c	0.0858 m
Rotor diameter	D	1.030 m
Span length	H	1.456 m
Swept area of rotor	A	1.236 m^2
Solidity	σ	0.25

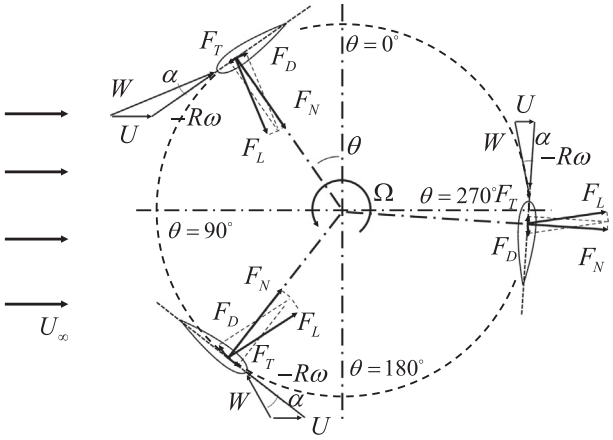

Fig. 2. The mechanical characteristics of the blade during one revolution.

$$W = \sqrt{(U_\infty + \lambda U_\infty cos\theta)^2 + (\lambda U_\infty sin\theta)^2} = U_\infty \sqrt{1 + 2\lambda cos\theta + \lambda^2} \tag{2}$$

The angle of attack α can be written as:

$$\alpha = \arctan\left(\frac{sin\theta}{\lambda + cos\theta}\right) \tag{3}$$

where θ is the azimuthal angle of the blade, and the region ranged from $\theta = 45°$ to $\theta = 135°$ is defined as the upwind region following the work of Ferreira and Geurts [53], from $\theta = 135°$ to $\theta = 225°$ is the leeward region, from $\theta = 225°$ to $\theta = 315°$ is the downwind region, from $\theta = 315°$ to $\theta = 45°$ is the windward region. Here λ is the tip speed ratio, defined as:

$$\lambda = \frac{R\Omega}{U_\infty} \tag{4}$$

The directions of tangential and normal forces, and the lift and drag are also shown in Fig. 2. The tangential force coefficient C_T and normal force coefficient C_N can be calculated as follows:

$$C_T = \frac{F_T}{\frac{1}{2}\rho c H W^2} \tag{5}$$

$$C_N = \frac{F_N}{\frac{1}{2}\rho c H W^2} \tag{6}$$

where F_T, F_N, ρ, c, H, and W are the tangential force, normal force, air density, chord length, span length and relative local velocity, respectively.

The power coefficient of the wind turbine is defined as:

$$C_P = \frac{Q\Omega}{\frac{1}{2}\rho U_\infty^3 A} \tag{7}$$

where Q, Ω, ρ, U_∞ and A are the rotor torque, angular velocity, air density, free-stream velocity, and swept area of the rotor, respectively.

Besides, the torque coefficient C_Q, thrust coefficient C_{thrust} and

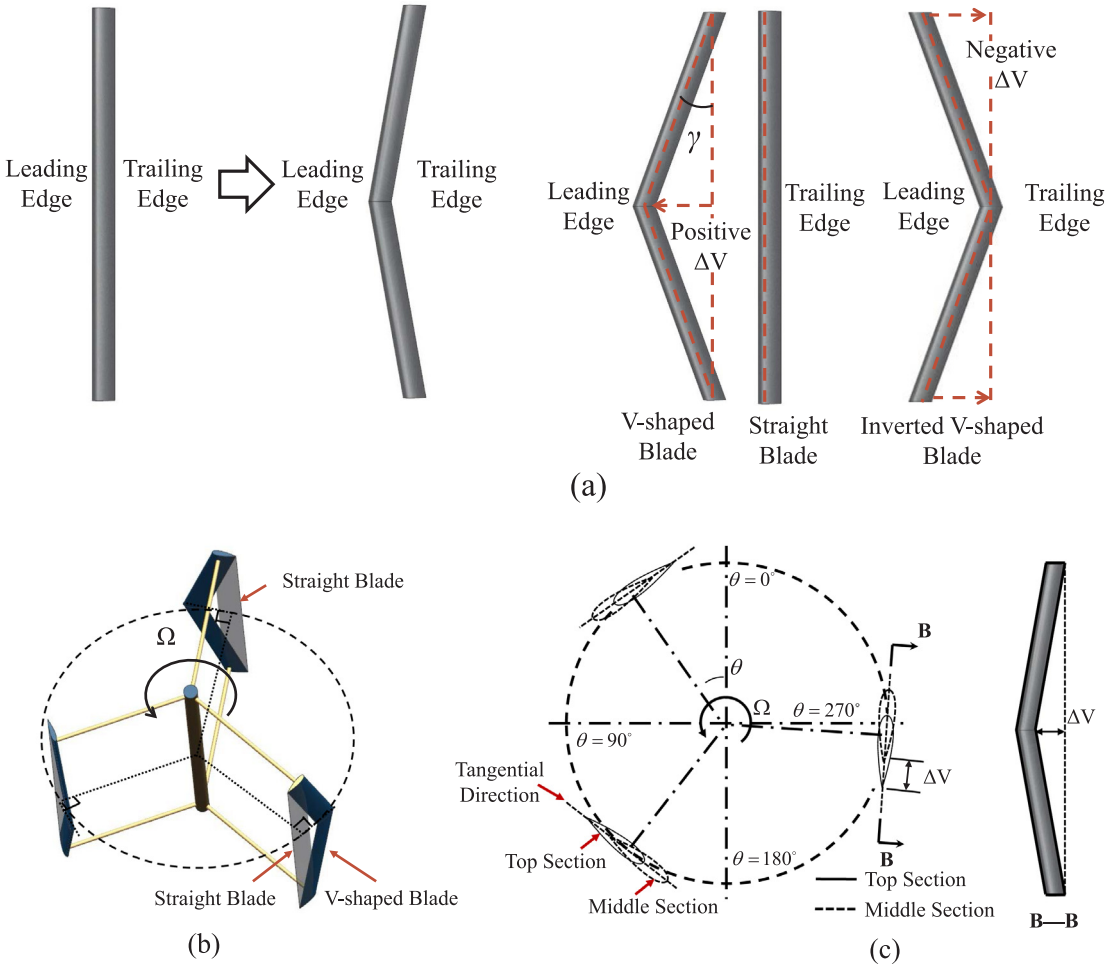

Fig. 3. The sketch map of the VAWT with V-shaped blade: (a) modification of the blade; (b) transformation of the three-dimensional model; (c) top view of the rotor.

lateral force coefficient $C_{lateral}$ can be defined as:

$$C_Q = \frac{Q}{\frac{1}{2}\rho U_\infty^2 AR} \tag{8}$$

$$C_{thrust} = \frac{F_{thrust}}{\frac{1}{2}\rho U_\infty^2 A} \tag{9}$$

$$C_{lateral} = \frac{F_{lateral}}{\frac{1}{2}\rho U_\infty^2 A} \tag{10}$$

And the directions of the thrust and lateral force are along stream-wise direction and cross-wind direction, respectively.

2.2. Schematic of the V-shaped blade

The sketch map of the VAWT with V-shaped blade is shown in Fig. 3. The position of the middle cross section of the blade moves forward (backward) along the tangential direction of the rotor, which may form an angle γ between the spanwise line and the vertical line (also called swept angle in aeronautics). The distance between the leading edge of the V-shaped blade and the leading edge of original straight blade is defined as ΔV, and the leading edge is kept parallel with the trailing edge for all blades. The averaged chord length of the V-shaped blades in spanwise direction is maintained as the same to that of the straight blade, which ensures the same solidity in all cases. Without increasing or decreasing the projected area of blade and rotor, the effects of moving distance ΔV on the blade middle section will be revealed in Section 4.

Besides, it should be noticed that for the rotor with V-shaped blade, the swept area increases in the middle part compared with the straight blade. The radius of the moving trajectory of V-shaped blade in the middle part can be calculated as:

$$R_{middle} = \sqrt{R^2 + \Delta V^2} \tag{11}$$

Thus, the increment of swept area ΔA is written as:

$$\Delta A = \frac{A_V}{A} - 1 = \frac{(R + R_{middle})H}{2RH} - 1 = \frac{\sqrt{1 + \frac{\Delta V^2}{R^2}} - 1}{2} \tag{12}$$

Because ΔV is much smaller than R, even for the max $\Delta V = 1.2c$ in the current study, ΔA calculated is only about 0.989%. This increment is small enough and the influence of the difference in swept area would be ignored in the study.

2.3. Computational domain and boundary conditions

As shown in Fig. 4, a three-dimensional computational domain was built to conduct the simulation. The length of the computational domain was 20D. The distance of the inlet boundary to the wind turbine center was 5D, and the outlet was located 15D downstream from the turbine center to make the flow field fully developed. The width and height of the computational domain were set as 10D and 4H, respectively. The sliding mesh technique was used to simulate the rotational motion of the VAWT. The computational domain was divided into a rotational region and a stationary region by setting interfaces. The data of the flow within these two regions were transferred through interfaces

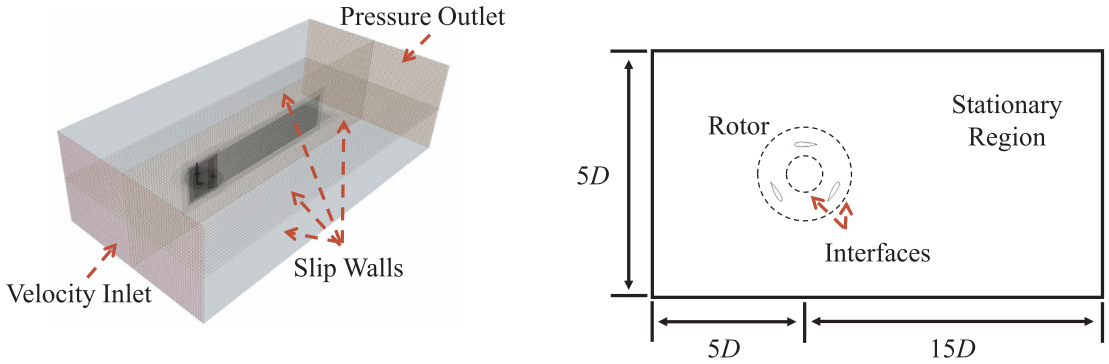

Fig. 4. The three-dimensional computational model and boundary conditions.

at each time step during the simulation. Besides, two refined regions were created to obtain the detailed information of the flow field. For the boundary conditions, the types of the inlet and outlet were set as uniform freestream velocity inlet and pressure outlet (0.0 Pa), respectively. The velocity of the free flow and the density of air were taken to be $U_\infty = 9$ m/s and $\rho = 1.225$ kg/m^3 with a turbulence intensity of 5 % in accordance to the experiments [19]. Finally, the other four sides of the computational domain were assumed as slip walls, while the surfaces of the blades were set as no-slip wall condition.

2.4. Numerical settings

The numerical settings utilized to solve the flow field are presented in this subsection. The three-dimensional unsteady incompressible flow was simulated by a finite volume-based CFD software STAR-CCM+ in this study. Implicit unsteady segregated flow method was chosen to solve the model. The SST $k-\omega$ turbulence model was utilized to solve the Navier-Stokes equations. The SST $k-\omega$ model has been widely applied in the aerospace industry, and it is suitable for solving the flow field around the wind turbine [51,54] due to its superiority in the solution of boundary layer flows.

The second-order upwind scheme was performed in the convection terms and the second-order central difference scheme was used for the temporal discretization. The SIMPLE algorithm was applied for coupling the pressure-velocity equation and the RANS model. The rotational motion of the VAWT was realized using sliding mesh. The azimuthal increment was set as 2°, which was proven to be sufficient for the simulation of VAWT [32,55]. Therefore, a determined time-step size $T/180$ (T is the period of one revolution) was employed during the calculation at different tip speed ratios, and 20 iterations were performed in each time step to ensure that the residuals were small enough. In each case, eight revolutions were calculated and data sampling for the average torque was conducted in the last two revolutions. All simulations were performed on a small-scale Server with two Intel(R) Xeon(R) CPUs (E5-2673 v3, 2.40 GHz), and about 168 h were taken to calculate the eight revolutions.

3. Numerical model validation

3.1. Mesh independence analysis

The mesh generation was performed in the software STAR-CCM+, where the trimmed mesher and prism layer mesher were utilized to generate volume meshes and orthogonal prismatic cells next to the wall surfaces of blades. To obtain an efficient mesh resolution scheme for the simulation, the mesh independence analysis was conducted with three computational meshes at the tip speed ratio $\lambda = 2.60$ where the maximum power coefficient C_P was obtained in the experiments. Fig. 5 illustrates the mesh topology and the boundary layer cells used in this study. The properties of the three meshes, named as coarse mesh, medium mesh, and fine mesh, are presented in Table 2. The main difference between three mesh schemes is the grid size around the blade. The minimum sizes of the grid around the blade are 12.5×10^{-4} m, 5.0×10^{-4} m, and 2.5×10^{-4} m corresponding to the coarse, medium, and fine mesh. For the boundary layer meshes, 30 layers of prismatic boundary layer cells with a total thickness of 0.0064 m were created. The growth ratio was set as 1.20 so that the wall function $y+$ during the calculation was approximately equal to 1. The Reynolds numbers calculated for this study are about $Re = 1.1 \times 10^5$~2.2×10^5.

Fig. 6 shows the instantaneous torque history for one blade during the last two revolutions. It can be observed that the torque curves of the medium mesh and fine mesh are almost overlapped while the torque of coarse mesh is lower. As shown in Table 2, the power coefficient C_P defined in Eq. (9) was used to evaluate the performance of the three mesh schemes.

The results show that with increasing the number of grids, lower error is obtained in the simulation. The average deviation of torque is small enough when the mesh is refined from medium to fine mesh, resulting in 1% errors in power coefficient. And the solution on the medium mesh is found to be sufficiently independent of mesh resolution. In this mesh topology, there are 170 points around the airfoil and 182 points along the spanwise direction. Thus, considering the computational time, all the rest of the simulations were based on the medium mesh scheme.

3.2. Validation

In order to evaluate the accuracy of the CFD results, the experimental measurements conducted by Castelli et al. [19] was used to validate the current model. The data of this experiment has been widely used in the investigation of aerodynamic performance of VAWT [51,17]. The validation study investigated a straight-bladed VAWT with three symmetric NACA0021 airfoils. The wind turbine operated at different tip speed ratios with the freestream velocity of 9 m/s and a turbulence intensity of 5%. The boundary conditions of the solution domain were set in line with that of the experiments to reproduce the experimental conditions as much as possible. All the other computational settings were kept as the same as described in Section 2.4. The target function, power coefficient C_P, was chosen to evaluate the results.

The comparison of the current results of C_P against experiments and numerical data [19,51] is shown in Fig. 7. It can be observed that the present study replicates the trend of power coefficient C_P versus tip speed ratio well, and a good agreement with the experiments can be found although small discrepancies are observed. Besides, it should be mentioned that after the experiment, only the data of average power coefficient versus tip speed ratio were published by the authors. Therefore, the dynamic torque coefficient variation obtained in the current study was also compared with that of the numerical results conducted by Castelli et al. [56] (see Fig. 8). It can be found that the present study successfully replicates the variation of instantaneous

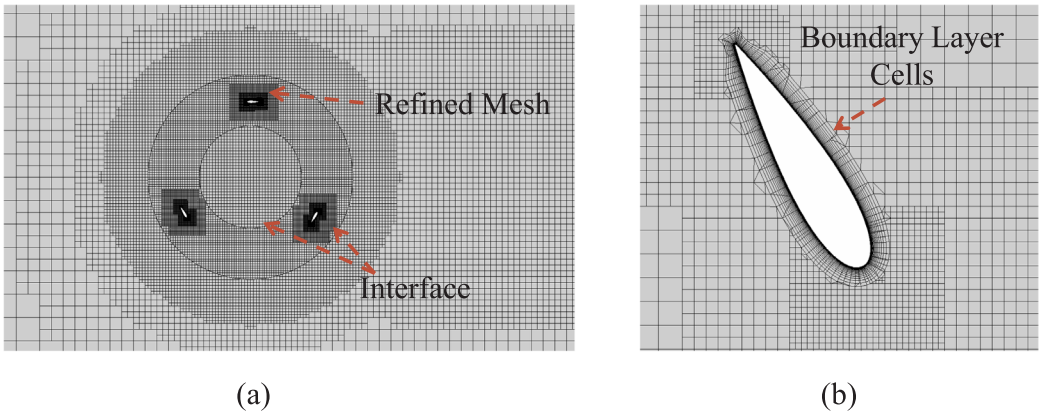

Fig. 5. The mesh topology at the cross section of the computational domain: (a) refined mesh; (b) boundary layer cells.

Table 2
Mesh topology around the blade.

Mesh Type	Minimum Grid Size	Total Number of Grids	Power Coefficient C_p
Coarse Mesh	12.5×10^{-4} m	7.8 million	0.2347
Medium Mesh	5.0×10^{-4} m	11.7 million	0.3023
Fine Mesh	2.5×10^{-4} m	13.7 million	0.3048

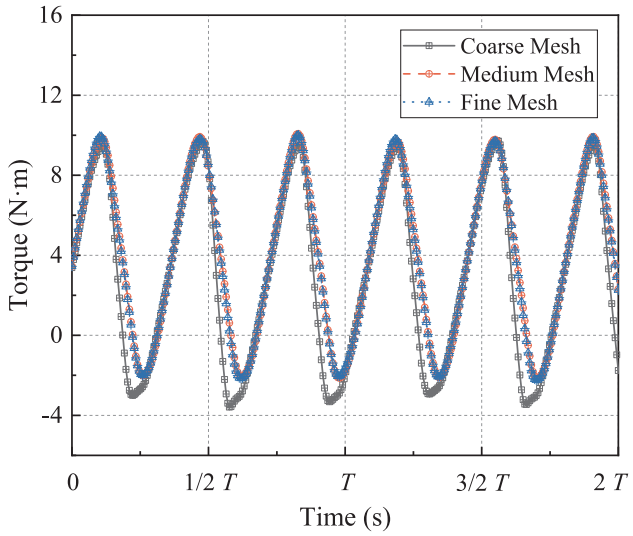

Fig. 6. The comparison of instantaneous torque history between three mesh schemes.

toque coefficient.

There is a small overestimation of power coefficient C_P for moderate to high tip speed ratios. This can be partly due to the geometric simplification of VAWT which can cause high obstruction effect at high rotational speeds. For low to moderate tip speed ratios, the calculated power coefficient C_P is relatively lower than the experimental data. It suggests that the model tends to underestimate the C_P at these operating conditions where the effect of geometric simplification is small. And this trend of underestimation of airfoil performance was also reported in the study by Ismail et al. [50].

Overall, based on the validation study, the numerical model is proved suitable to reflect the aerodynamic characteristics of the VAWT in wind tunnel, and is able to accurately replicate the experimental results. Therefore, it suggests that the current numerical model can be applied as a reliable approach in the simulations in following studies.

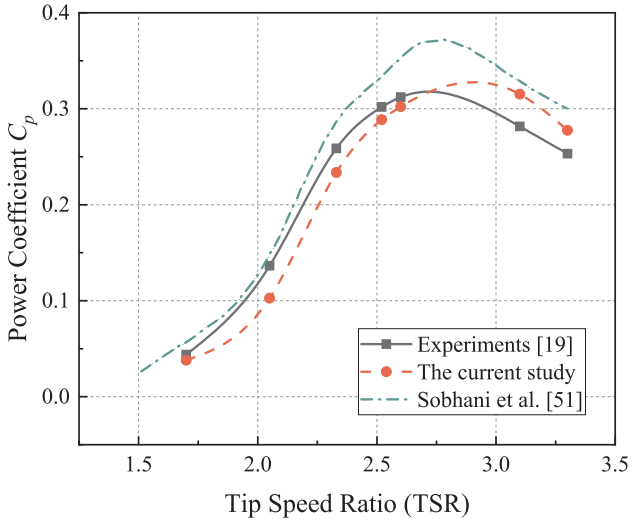

Fig. 7. Comparison of the current results against experimental and numerical data [19,51].

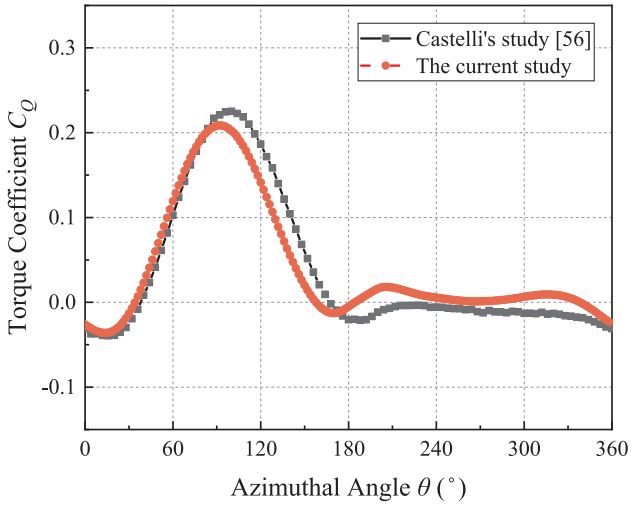

Fig. 8. Comparison of the dynamic toque coefficient at tip speed ratio $\lambda = 3.1$ [56].

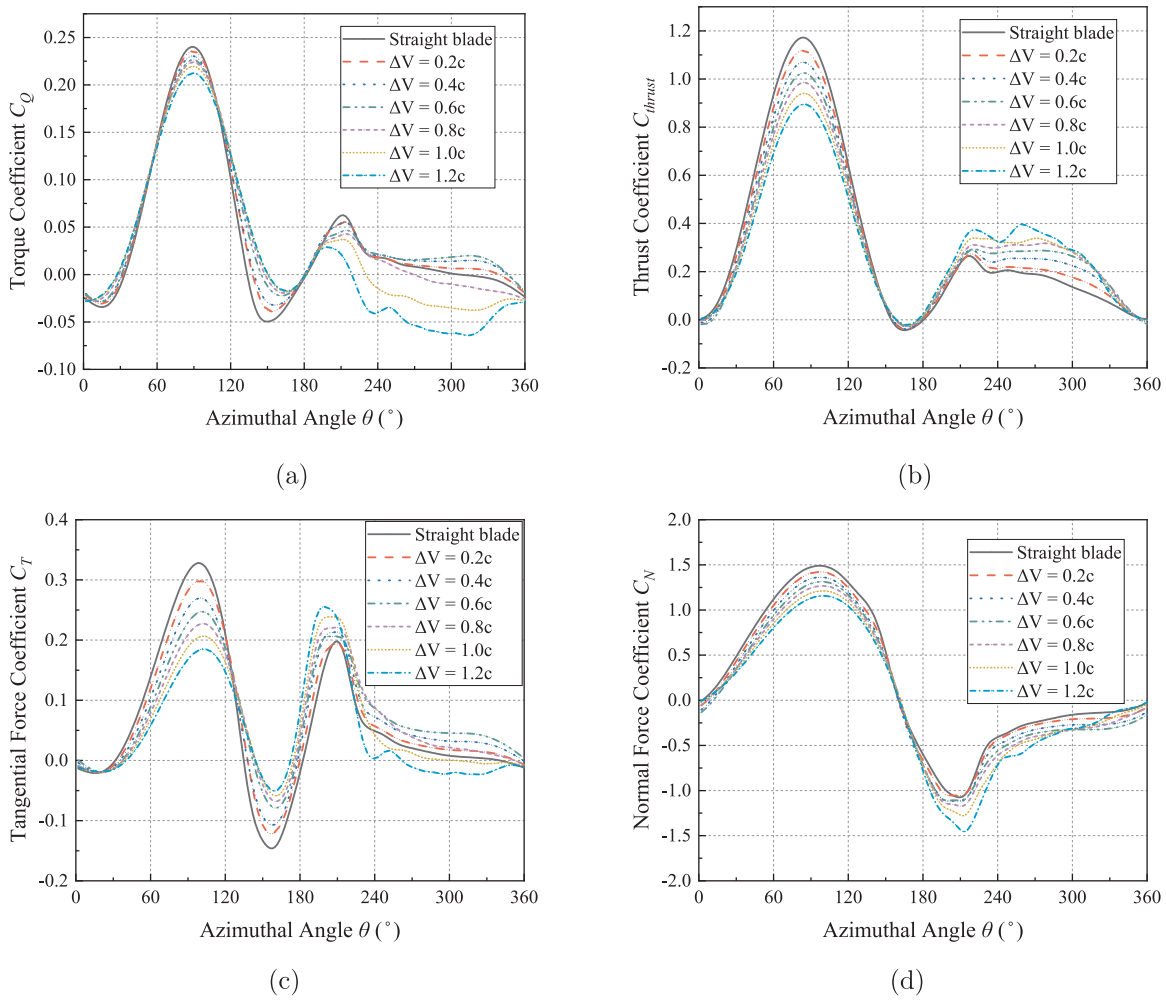

Fig. 9. The variations of the force coefficients versus azimuthal angle for different V-shaped blades: (a) torque coefficient C_Q; (b) thrust coefficient C_{thrust}; (c) tangential force coefficient C_T; (d) normal force coefficient C_N.

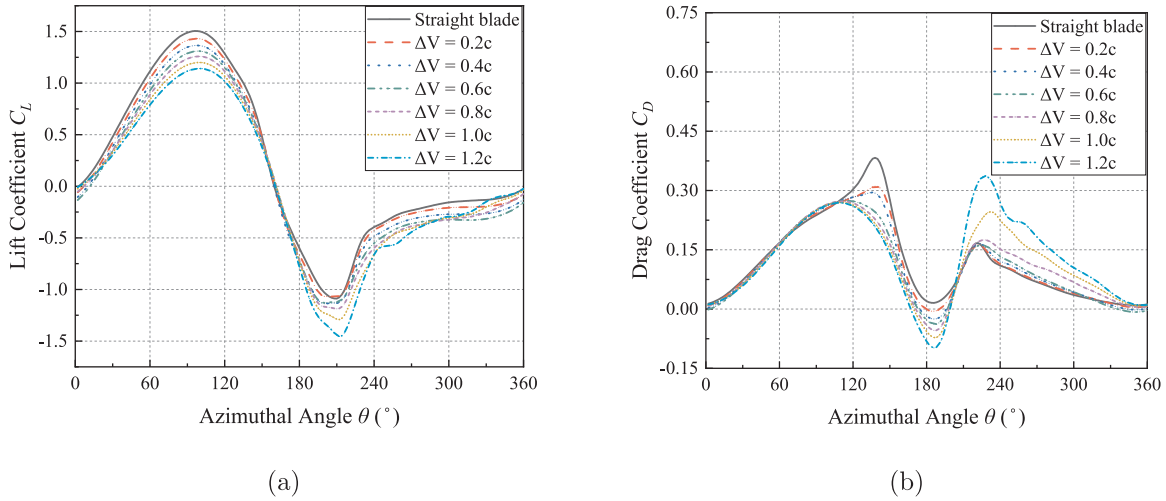

Fig. 10. Comparison of the lift and drag coefficients versus azimuthal angle for different V-shaped blades: (a) lift coefficient C_L; (b) drag coefficient C_D.

4. Results and discussions

4.1. Aerodynamic performance

The aerodynamic loads on the wind turbine are the main parameters to measure its aerodynamic performance. The variations of the force coefficients for different V-shaped blades are illustrated in this section. Fig. 9(a) shows the variations of the torque coefficient versus azimuthal angle at tip speed ratio $\lambda = 2.60$. It can be observed that the V-shaped configurations change the distribution patterns of the torque coefficient C_Q in the revolution. In most of the upwind region, all the torque coefficients of V-shaped blades are lower than that of the straight blade,

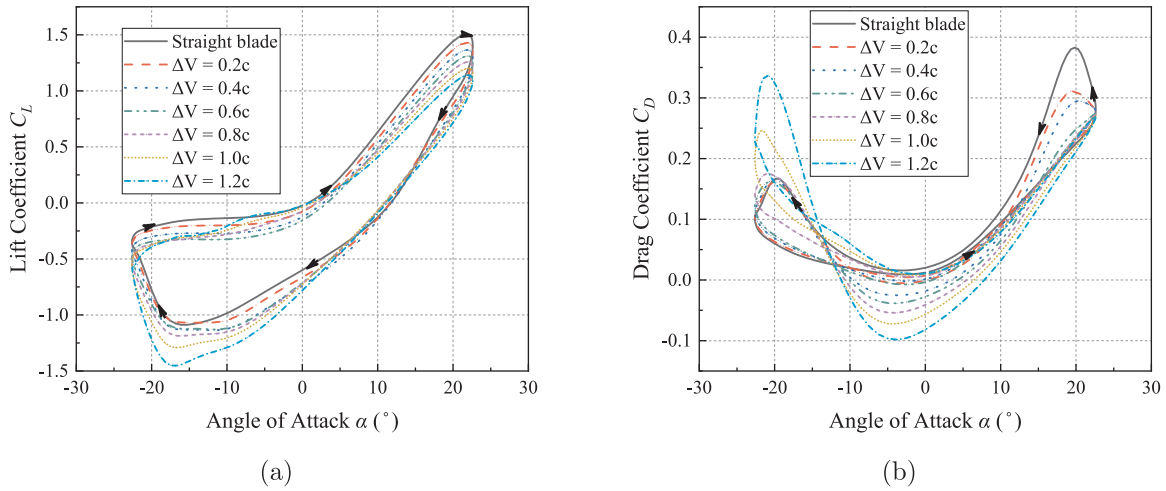

Fig. 11. The variations of the lift and drag coefficients versus angle of attack for different V-shaped blades: (a) lift coefficient C_L; (b) drag coefficient C_D.

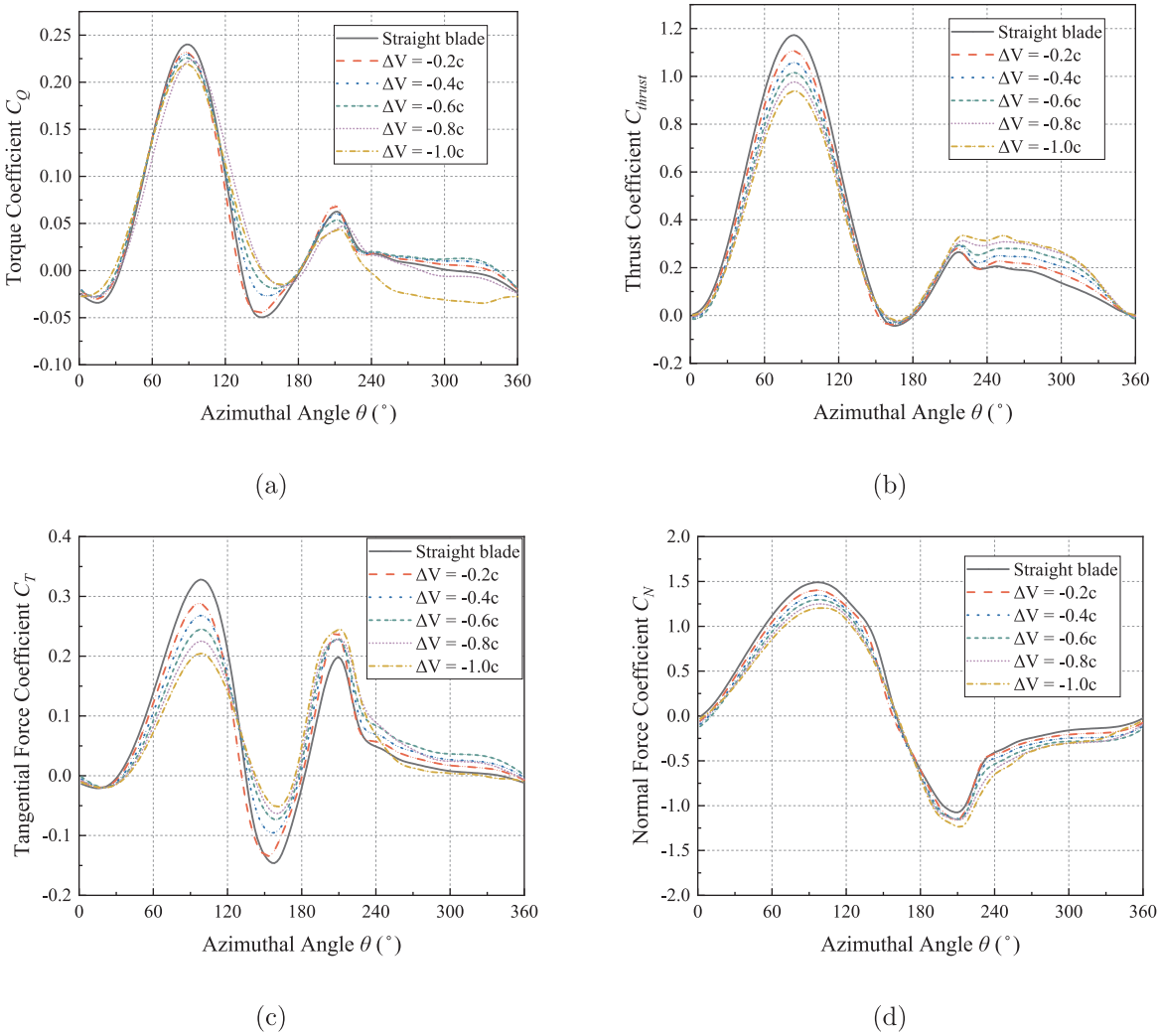

Fig. 12. The variations of the force coefficients versus azimuthal angle for the inverted V-shaped blades: (a) torque coefficient C_Q; (b) thrust coefficient C_{thrust}; (c) tangential force coefficient C_T; (d) normal force coefficient C_N.

and the larger moving distance ΔV results in lower C_Q. In this region, the difference of C_Q for $\Delta V = 0.6c$ and $\Delta V = 0.8c$ is small. The peak value of C_Q for $\Delta V = 0.6c$ is 0.226 occurring at $\theta = 90°$ while the peak value of C_Q for $\Delta V = 0.8c$ is 0.224 at $\theta = 90°$. The minimum peak value of C_Q is 0.212, which occurs on $\Delta V = 1.2c$ at $\theta = 90°$. On the contrary, in a small part of the upwind region and half of the leeward region ($115° \leqslant \theta \leq 180°$), V-shaped blades effectively improve the performance of the wind turbine. Moving distance ΔV actually results in higher torque coefficient, and when ΔV is raised up to $0.6c$, the increment of torque decreases. This is mainly due to the sudden increase in the drag

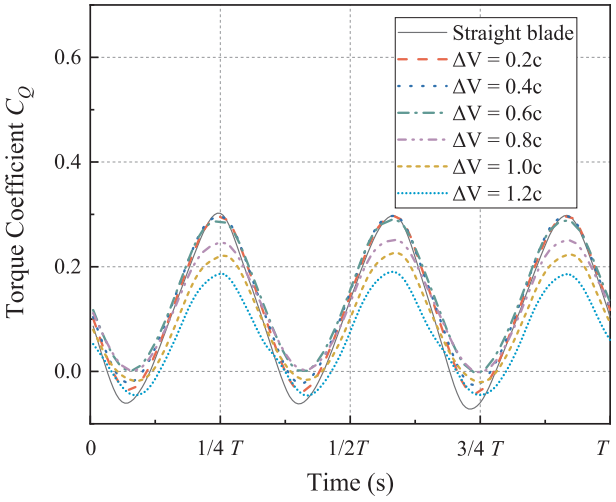

Fig. 13. Comparison of the fluctuation of the torque coefficient of the whole rotor with three blades.

coefficient which would be illustrated later. In the downwind and windward regions ($225° \leqslant \theta \leq 45°$), the V-shaped blades show both the positive and negative effects which should be clarified separately. For $\Delta V = 0.2c$, $\Delta V = 0.4c$ and $\Delta V = 0.6c$, the positive effects on torque coefficient are observed all over the downwind and windward regions, among which $\Delta V = 0.6c$ has shown the best performance. And it can be found that the major positive value of the power output made by a single blade is generated from the region $30° \leqslant \theta \leq 150°$ and $180° \leqslant \theta \leq 340°$. On the other hand, a higher positive value of ΔV, including $\Delta V = 0.8c$, $\Delta V = 1.0c$ and $\Delta V = 1.2c$, results in more power loss in the region from $\theta = 225°$ to $\theta = 5°$ comparing with the baseline model, while a little benefit can be found from $\theta = 5°$ to $\theta = 50°$. Considering the overall performance of V-shaped blade with different distances ΔV, therefore, higher positive values of $\Delta V \geqslant 1.2c$ are not analyzed in the present study.

The comparison of the thrust coefficient variations versus azimuthal angle for different V-shaped blades are shown in Fig. 9(b). Similar to the instantaneous torque coefficient, the V-shaped configuration makes a shift in the thrust coefficient C_{thrust} in the revolution. The thrust coefficient of V-shaped blade is lower than that of straight blade in the fore half ($0° \leqslant \theta \leq 180°$) while the value of C_{thrust} is higher compared with the baseline model for $180° \leqslant \theta \leq 360°$ in the revolution. This is different from the trend of C_Q, where the decrease in C_Q from $\Delta V = 0.8c$ to $\Delta V = 1.2c$ is not observed for C_{thrust}. Conversely, the larger distance ΔV results in higher C_{thrust} in this region.

The effects of distance ΔV for V-shaped VAWT on blade tangential force coefficient C_T and normal force coefficient C_N are presented in Fig. 9(c) and (d). The direction of the tangential force is along the chord line from the trailing edge to the leading edge because there is no pitch angle considered in the current study. The normal force is perpendicular to the tangential force and points to the center of the rotor. In the most of the fore ($0° \leqslant \theta \leq 180°$) and aft ($180° \leqslant \theta \leq 360°$) halves of the revolution, the normal force coefficient C_N of V-shaped blade is lower than that of straight blade. In the windward region, however, the

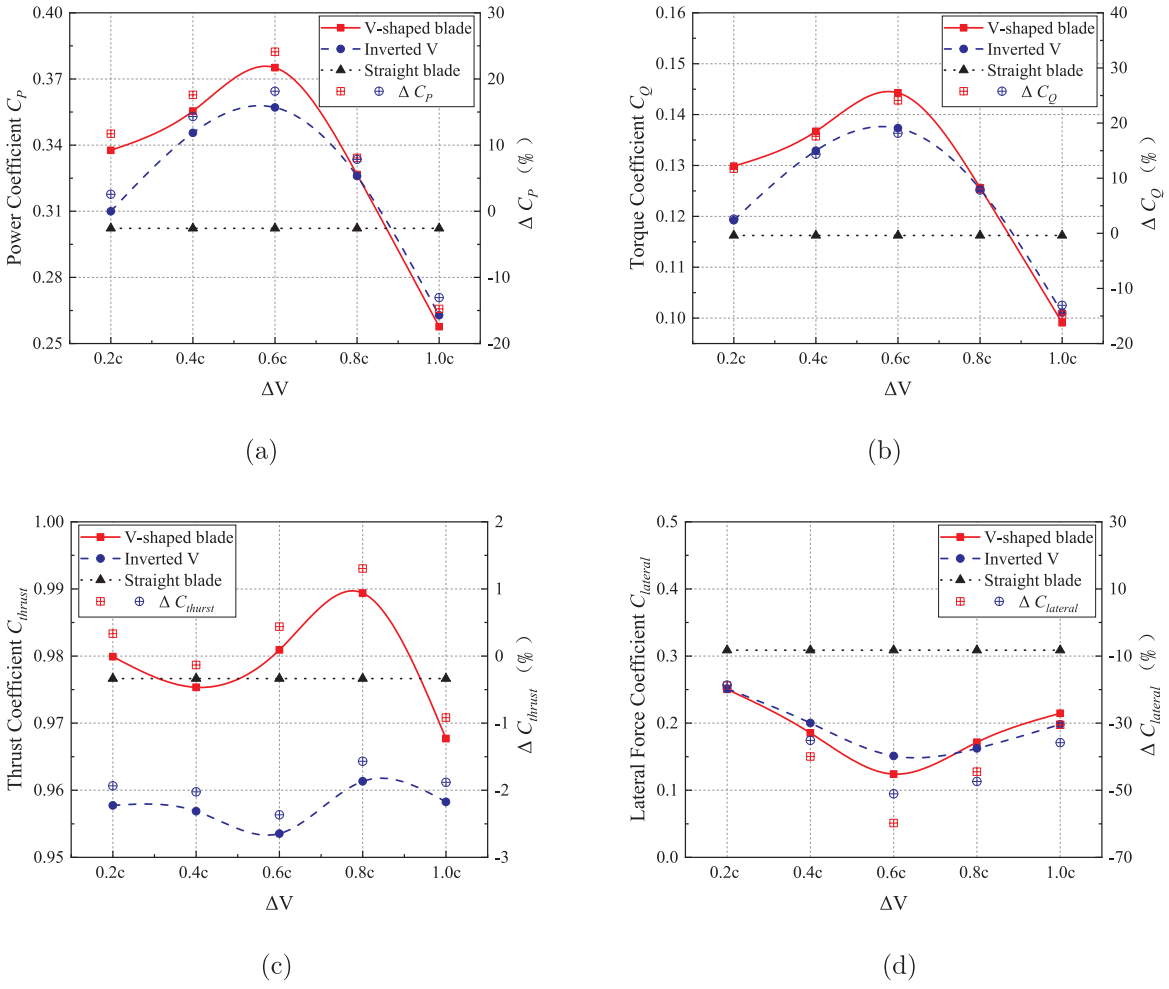

Fig. 14. Comparison of (a) power coefficient C_P, (b) torque coefficient C_Q, (c) thrust coefficient C_{thrust}, and (d) lateral force coefficient $C_{lateral}$ for different blades.

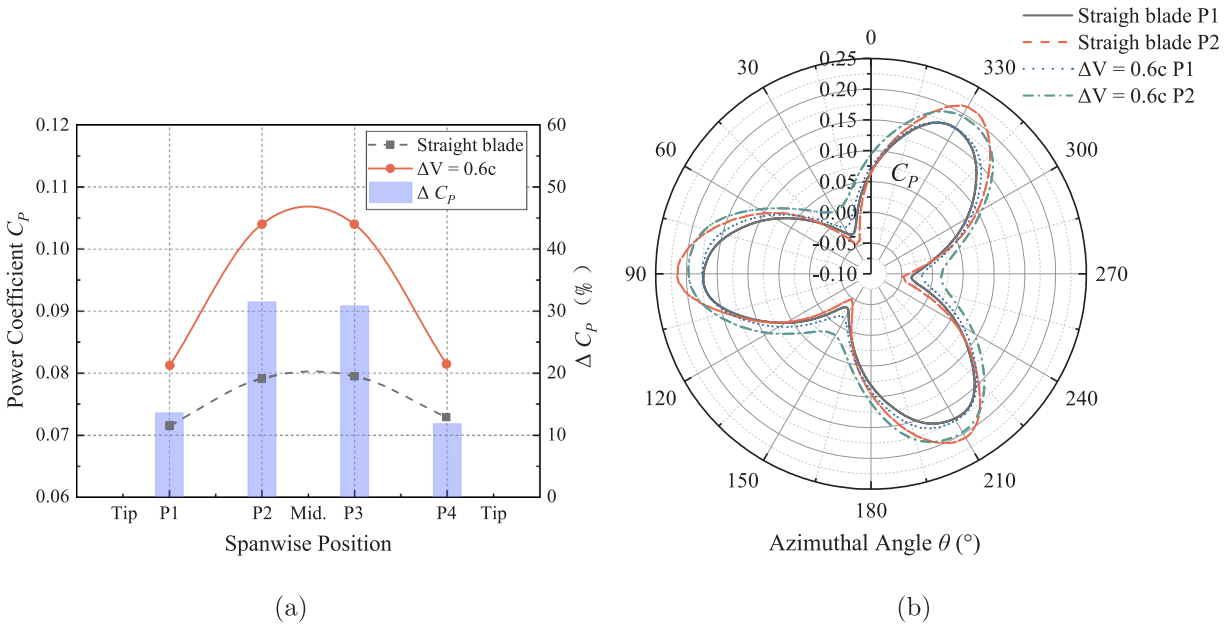

Fig. 15. Comparison of power coefficient of each part for different blades: (a) average power coefficient; (b) instantaneous power coefficient.

normal force coefficients for $\Delta V = 0.8c$, $\Delta V = 1.0c$, and $\Delta V = 1.2c$ increase a lot while the minimum value of C_N occurs at $\Delta V = 0.6c$. On the other hand, the variations of tangential force coefficient are different. In the fore half of the revolution, the V-shaped blade causes lower tangential force coefficient in the upwind region while a higher coefficient value is found in the leeward region. This trend is similar with that found in the blade camber effect [14]. It indicates that energy extraction for the V-shaped blade is more balance between the fore and aft halves of the revolution compared with the straight blade. In the downwind region, distance ΔV has different effects on the tangential force coefficient. The distance ΔV from $\Delta V = 0.2c$ to $\Delta V = 0.8c$ benefits the tangential force coefficient, among which $\Delta V = 0.6c$ is the optimal one, while $\Delta V = 1.0c$ and $\Delta V = 1.2c$ result in the reduction of C_T in this region. It suggests that similar to the pitch angle controlling strategies in the work of [17,57], only a certain value of distance ΔV can obtain the optimal performance.

To make further investigation on the physics behind the shift in the torque coefficient variations, the lift and drag coefficients are calculated. Fig. 10 illustrates the lift and drag coefficients versus azimuthal angle θ at tip speed ratio $\lambda = 2.60$. It can be observed that when the rotor start operating the lift coefficient of the blade increases gradually and the maximum value of lift coefficient C_L occurs at an earlier azimuthal position than angle of attack α. After that, an obvious dynamic stall can be found for the straight blade (black solid line), where a reduction in lift coefficient and a sudden increase in drag coefficient happen at about $\theta = 120°$. In the aft half of the revolution, another stalling can be observed from $\theta = 210°$ to $\theta = 224°$ for the baseline model. Comparing with that, the V-shaped blade can effectively reduce the negative effect of dynamic stall. In the upwind region, the distance ΔV of the V-shaped blade makes lower C_L compared with straight blade. Meanwhile, the V-shaped configuration significantly reduces the drag coefficient and eliminates the local mutation of drag coefficient from $\theta = 115°$ to $\theta = 180°$. It explains the improvements on torque coefficient caused by the V-shaped blade in this region. Then in the aft half of the revolution, the direction of the lift force changes and the absolute value of lift coefficient is increased with ΔV. For the drag coefficient, however, the effect of V-shaped configuration should be discussed separately. From $\theta = 180°$ to $\theta = 205°$, all the drag coefficients of V-shaped blades are lower than that of straight blade. After that, the drag coefficients increase a lot and return to the same level as the baseline model. For ΔV from $0.2c$ to $0.6c$, the drag coefficients are slightly larger than the baseline blade, while for ΔV from $0.8c$ to $1.2c$ the drag coefficients increase dramatically resulting in more severe dynamic stall phenomena. Besides, it should be noticed that the absolute lift coefficients of the V-shaped blade with ΔV from $0.8c$ to $1.2c$ decrease sharply and no benefit is found for lift coefficient C_L in the windward region. The reason is that in this region the flow separation is more likely to occur at the tip of the blades with high values of ΔV due to the cross-flow along the span.

The variations of lift and drag coefficients versus angle of attack at tip speed ratio $\lambda = 2.60$ are shown in Fig. 11. A large hysteresis effect can be found in the force coefficient history. The lift coefficients of the V-shaped blade increase linearly with the angle of attack for all cases. And all of these are lower than that of the baseline model in the upstroke motion. After that, they are almost overlapped until the blade rotates to the downwind region. In the negative angle of attack region, the absolute lift coefficients of the V-shaped blade are higher than that of the straight blade. And the blade is affected by the dynamic stall earlier at a smaller absolute angle of attack in the downstroke motion. On the other hand, it is observed that the maximum drag coefficient of the straight blade occurs after the maximum angle of attack is reached. It is clear that the drag coefficients of the V-shaped blade are much lower than that of the baseline model in the fore half of the revolution. It is due to the effect of V-shaped blade on suppressing flow separation, which is also confirmed in the vorticity distribution around the blade discussed later. However, the negative effect on drag coefficient can be found in the V-shaped blade with higher values of ΔV in the negative angle of attack region.

The variations of the torque coefficient C_Q versus azimuthal angle for different inverted V-shaped blades at the tip speed ratio $\lambda = 2.60$ are presented in Fig. 12(a). For the inverted V-shaped blade, the distance ΔV is set from $\Delta V = -0.2c$ to $\Delta V = -1.0c$ according to the previous results. Similar to Fig. 9(a), the inverted V-shaped blades also show the trend of changes in C_Q in the revolution although quantitative differences are observed at certain positions. All the torque coefficients of inverted V-shaped blades are lower than the baseline model in the upwind region. The peak value of C_Q for $\Delta V = -0.6c$ is 0.226 at $\theta = 88°$ while the peak value of C_Q for $\Delta V = -0.8c$ is 0.223 at $\theta = 90°$. In the leeward and windward regions, all curves show similar trends as illustrated before, except for the value of the inverted V-shaped blade

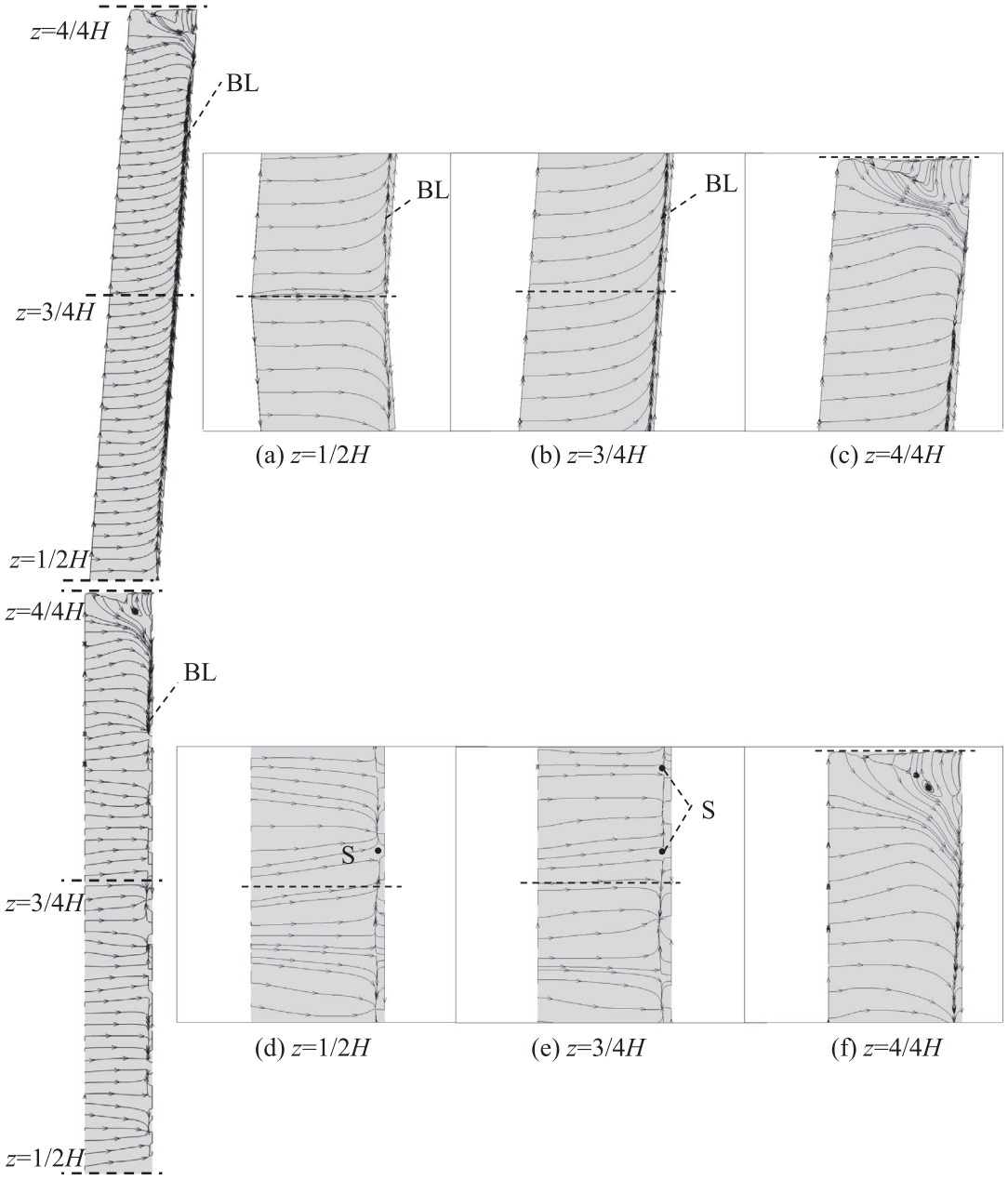

Fig. 16. Comparison of time-averaged streamline patterns Ψ on blade surface: bifurcation line, *BL*; saddle point, *S*; (a) V-shaped blade; (b) straight blade.

$\Delta V = -0.2c$, which is higher than the straight blade from $\theta = 200°$ to $\theta = 218°$. In the downwind region, when the negative distance ΔV is decreased to $\Delta V = -1.0c$, the lower torque coefficient is found, implying that the more negative distance ΔV will further damage the performance of VAWT. The effect of the (inverted) V-shaped configuration on the torque coefficient in the upwind region is similar with the trend found in pitch angle research [17], namely the baseline straight blade makes the highest C_Q within this region. Besides, in the downwind region, negative pitch angles cause higher torque coefficient and positive pitch angles make lower torque coefficient. However, for the V-shaped VAWT, both the negative and positive values of ΔV can improve the torque coefficient in a certain range. In addition, it should be noticed that the less torque fluctuation generated by V-shaped blade in the revolution (see Fig. 13) will make the torque coefficient curve of the whole VAWT smoother, which to some extent, achieves the similar effect as helical blade does [46], namely, to minimize rotor vibrations and stabilize the performance.

Similarly, the thrust coefficient, tangential coefficient and normal coefficient versus azimuthal angle for the inverted V-shaped blades are investigated. There is no major change in the behaviors of these dynamic loads compared with the V-shaped blade. As shown in Fig. 12, for the thrust coefficient of the single inverted V-shaped blade, two peaks appear both in the upwind and downwind region. Smaller negative ΔV results in lower thrust coefficient in the upwind region and generates a larger value in the aft half of the revolution. Fig. 12(c) and (d) show the tangential and normal force coefficient variations of the inverted V-shaped blade. The history of C_T and C_N resembles what was found in the case of positive ΔV for the most of rotating process. However, it can be observed that the maximum tangential force coefficient of the inverted V-shaped blade occurs at an earlier azimuthal position and is lower than that of the V-shaped blade.

Fig. 14(a) and (b) show the comparisons of average power coefficient and torque coefficient obtained from different V-shaped configurations in the last two revolutions. From the results it is clear that the

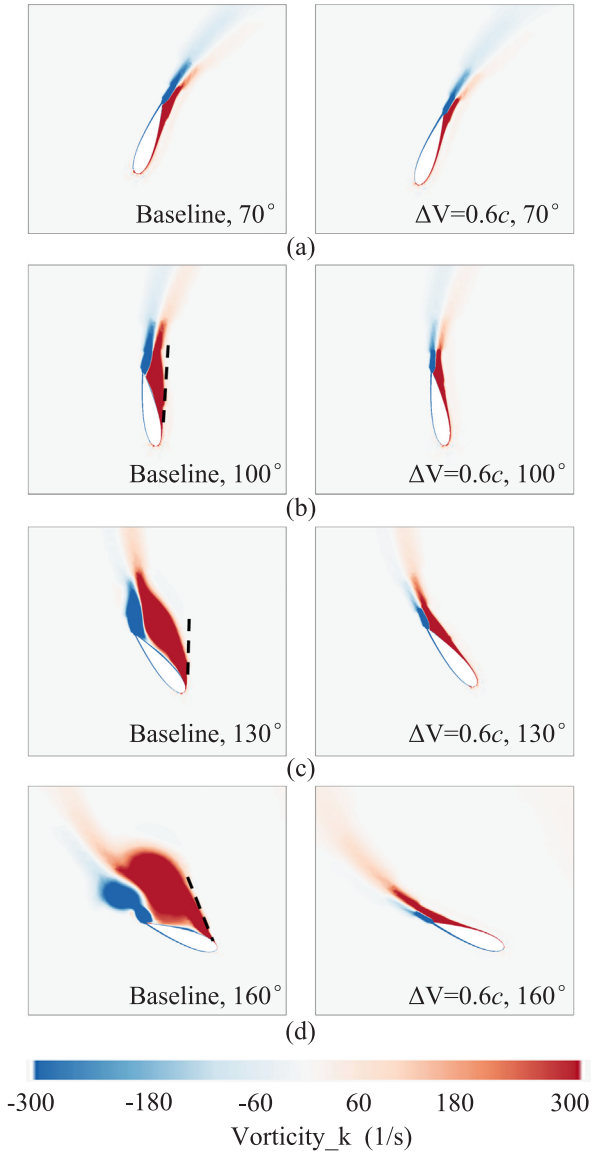

Fig. 17. The comparison of vorticity distributions at the middle section around two blades: (a) $\theta = 70°$; (b) $\theta = 100°$; (c) $\theta = 130°$; (d) $\theta = 160°$.

value ΔV of V-shaped blade has an important impact on the power performance of wind turbine. Both for the V-shaped blade and the inverted V-shaped blade, increasing the absolute value of ΔV will improve the performance of VAWT, and the optimum power outputs occur at $\Delta V = 0.6c$ and $\Delta V = -0.6c$, respectively. After that, the effect of increasing the absolute value of V on performance improvements decreases and even the performance degradations happen at $\Delta V = \pm 1.0c$.

To find out which part of the modified V-shaped blade contributes to the power improvement of VAWT, the blades are divided into four equal parts along the spanwise direction to compare the performance of power output. Here, only the straight blade and the V-shaped blade with $\Delta V = 0.6c$ which achieves the maximum power outputs are investigated. The average values and variations of power coefficients of different parts of the blade are illustrated in Fig. 15. Among the four separate blade segments, the segments containing the blade tip are named as P1 and P4, while those containing the middle part of the blade are P2 and P4, respectively. It can be found that most positive power outputs are attributed to the middle segments of the blade, while blade tip effect results in lower power coefficient near the blade tip. For the VAWT with V-shaped blade, the aerodynamic performance is improved for all segments of the blade, and the main enhancement is also found in the middle parts of the blade where the power coefficient is about 31% higher than that of the straight blade.

The comparison of the thrust coefficient can be found in Fig. 14(c). It indicates that the V-shaped blade has a small effect on C_{thrust}, and a similar conclusion was reached in the behavior of pitch angle controlling by Simão Ferreira and Scheurich [58]. For the (inverted) V-shaped blade, the relative change in C_{thrust} with different ΔV is less 5% which is much smaller than those for C_P and $C_{lateral}$. This is contrary to the findings by Rezaeiha et al. [17] in which the higher value of C_{thrust} was associated with a higher C_P. To confirm the relationship between the thrust coefficient C_{thrust} and power coefficient C_P, further research is needed in the future.

A further novel finding is that the V-shaped configuration effectively reduces the average lateral loads on the wind turbine as shown in Fig. 14(d). The total aerodynamic load applied to the turbine can be divided in both the streamwise and cross-stream directions [59]. Although the lateral force is one of the main parameters in the evaluation of structural strength, vibration and fatigue damage performance [59–61], the wind turbine blade optimization in previous studies had little effect on reducing the lateral force [17] except for the investigation of the number of blades [62]. In the current study, the lateral force coefficients $C_{lateral}$ at the optimum value of $\Delta V = 0.6c$ for the V-shaped blade and $\Delta V = -0.6c$ for the inverted V-shaped blade are approximately 59% and 51% lower than that of the baseline model. This configuration reduces the damage to the wind turbine caused by lateral loads to a certain extent which was rarely mentioned in the previous studies.

4.2. Flow structure

Time-averaged streamline patterns Ψ on the V-shaped blade surface and straight blade surface are illustrated in Fig. 16. Based on the previous results, only the baseline model and the V-shaped blade with $\Delta V = 0.6c$ are investigated in the following sections, and the time-averaged streamline patterns on the suction side of the V-shaped blade and straight blade calculated during the fore half of the revolution ($0° \leqslant \theta \leq 180°$) are used to represent the flow structure on blade surface. In the time-averaged streamline topology, it can be observed that a line of separation, indicated by a negative bifurcation line *BL*, appears both on the suction side of two blades. It is notable that the negative bifurcation line *BL* on the V-shaped blade is closer to the trailing edge compared with that on the straight blade. This is in line with the results obtained in Section 4.1 and elucidates that the straight blade suffers more severe dynamic stall at sufficient high angle of attack. For the straight blade, several saddle points *S* [63] can be found on blade surface (see Fig. 16(d) and (e)), reflecting the irregular and complex cross-flow structures along the spanwise direction. And it also demonstrates the higher drag coefficient observed in the revolution for the baseline model. Besides, the time-averaged streamlines Ψ distributed in the blade tip region are shown in Fig. 16(c) and (f). It suggests that the flow structure in the blade tip region of the V-shaped blade is similar to that of the baseline model. And this will also be confirmed later in the static pressure distributions.

As shown in Fig. 17, the comparison of vorticity distributions at the middle section $z = 1/2H$ around two blades are illustrated to visualize the formation and development of the flow separation. It can be observed that the flows are basically attached to the blade surface for both two models at the azimuthal angle $\theta = 70°$. When the blade rotates to the position $\theta = 100°$, a mild flow separation can be found on the suction side of straight blade surface shown in Fig. 17(b). After that the trailing edge separation point gradually moves forward and the strengths of trailing edge and leading edge vortices increase a lot, indicating the severe dynamic stall occurred at these positions. It also corresponds to the sharp decrease in the torque coefficient in Fig. 9. On the contrary, the V-shaped blade shows superiority in suppressing flow separation. At the position $\theta = 130°$ and $\theta = 160°$ (see Fig. 17(c) and

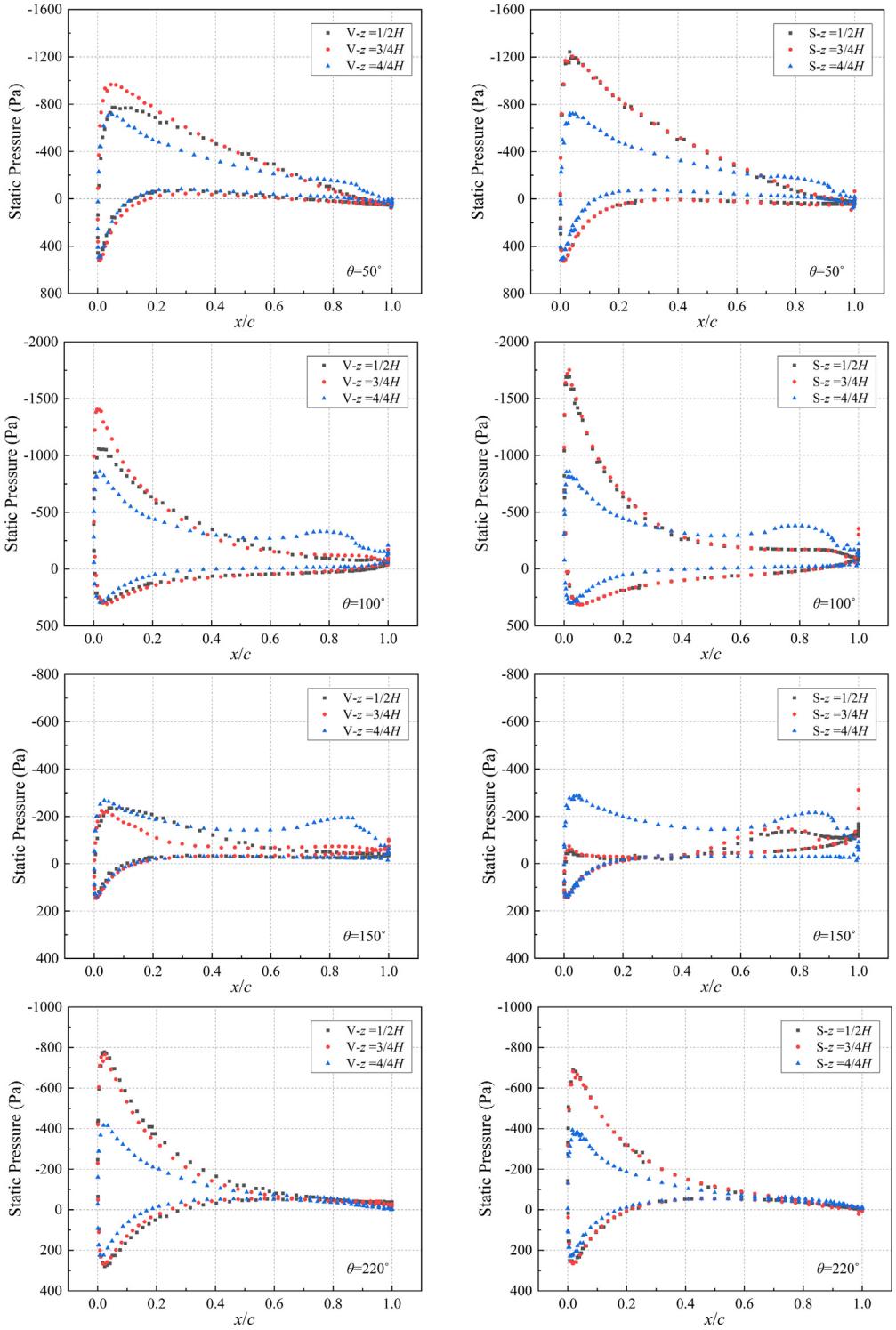

Fig. 18. The static pressure distributions on blade surface: the section of V-shaped blade, V-z; the section of straight blade, S-z.

(d)), the flow separations on the V-shaped blade surface are effectively suppressed and the strength of shedding vortices are relatively smaller. A similar pattern of results was obtained in study of swept wing by Medina et al. [64]. And it is consistent with the torque coefficients on the blades shown in Fig. 9(a).

4.3. Static pressure distribution

The static pressure distributions at the middle section, the 3/4 span section and the top section are shown in Fig. 18. It can be found that in the upwind region ($45° \leqslant \theta \leq 135°$), the straight blade results in a higher negative pressure in the leading edge except for the top section. However, the pressure distribution pattern changes in the leeward and downwind region ($150° \leqslant \theta \leq 330°$). At the middle and the 3/4 span sections, the higher negative pressure can be observed on the V-shaped blade surface while the positive pressure is almost the same. This greater pressure difference between the pressure side and the suction side results in higher lift coefficients mentioned in Section 4.1. Besides,

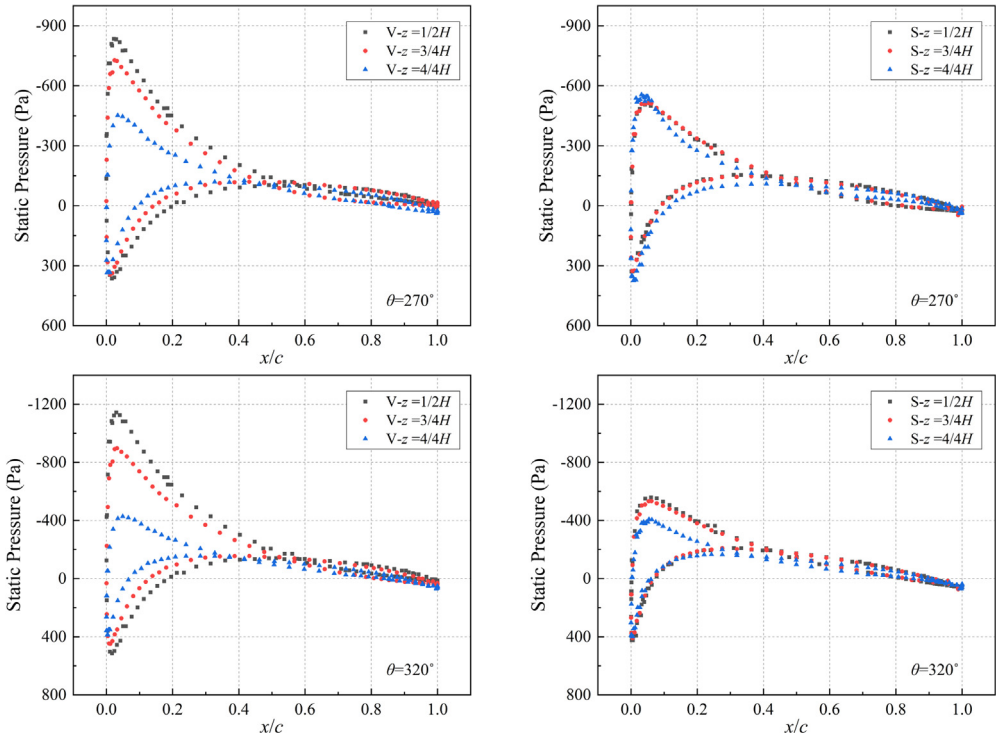

Fig. 18. (*continued*)

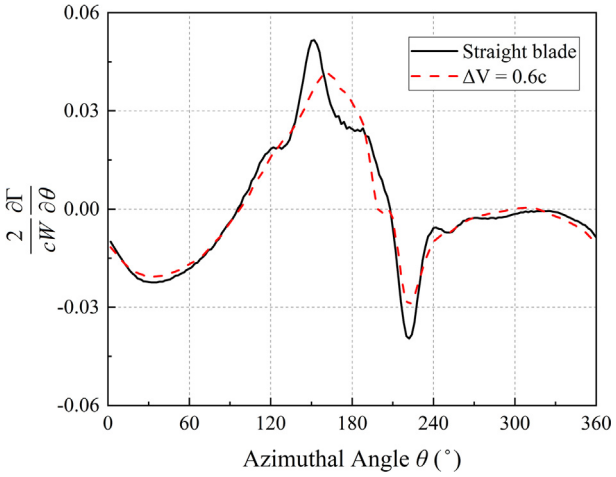

Fig. 19. Shed vorticity by a single blade over the last revolution.

the tip vortex effect can be clearly observed at the azimuthal angle $\theta = 100°$ and $\theta = 150°$ where the presence of the vortex causes a distinctive pronounced suction region similar to the findings by Lombard et al. [65]. In the aeronautic engineering, it is generally considered that the pressure difference between the blade root and blade tip promotes the cross-flow and makes the boundary layer thicker at the blade tip, which is prone to flow separation at subsonic speed [66]. It is suggested that the V-shaped blade might also have deficiency in the blade tip effect compared to the straight blade at subsonic speed due to the stronger cross-flow. However, there is only a little difference between the pressure distributions at the top section of two kinds of blades as shown in Fig. 18. This might be due to the low freestream velocity and low swept angle of blade in the current study which keeps the advantages of V-shaped blade in lifting and drag coefficients, and prevents V-shaped blade form suffering stronger blade tip effect.

4.4. Wind turbine wake

The movement and development of the shedding vortices form the wind turbine wake. Based on the Kutta-Joukowski theorem and the definition of the lift coefficient [67], the connection between the circulation around the blade and lift coefficient is built up. The unsteady circulation Γ means the continuous vortex shedding from the blade. And the shedding vortex has strength equal and opposite to the rate of change of circulation per azimuthal angle [67], written as:

$$\frac{\partial \Gamma}{\partial \theta} = -\frac{1}{2} U_\infty c \frac{\partial C_L}{\partial \theta} \tag{13}$$

Thus, in the current study, calculated by the simplified local velocity W, the non-dimensional form of Eq. (14) is provided in [53] as follows.

$$\frac{2}{cW}\frac{\partial \Gamma}{\partial \theta} = -\frac{\partial C_L}{\partial \theta} \tag{14}$$

Fig. 19 shows the strength of the shedding vortex of a single blade over the last revolution for the straight blade and V-shaped blade, where the positive value indicates counter-clockwise circulation. It can be observed that in the upstroke motion of the blade where C_L increases shown in Fig. 11(a), clockwise vortices shed corresponding to the curves with negative value, while counter-clockwise vortices shed during the downstroke motion. And it can be found that the V-shaped blade reduces the strength of the shedding vortex, which might be due to the flow separation suppression illustrated in Fig. 17.

To ensure the wind turbine wake fully developed, more revolutions of the rotor are needed in the study [68,16]. And the streamwise velocity distribution was monitored for checking the convergence of wake properties [69]. Fig. 20 shows the averaged streamwise velocity distributions at distances of $X = 4D$ and $X = 6D$ with different revolutions. It can be observed that the far wake takes much more time to reach a state of full development compared to the near wake. Besides, it can be seen that after 20 revolutions, the far wake achieves the convergence in the streamwise velocity distribution which can be used in the following investigation.

The profiles of averaged streamwise velocity distribution of the

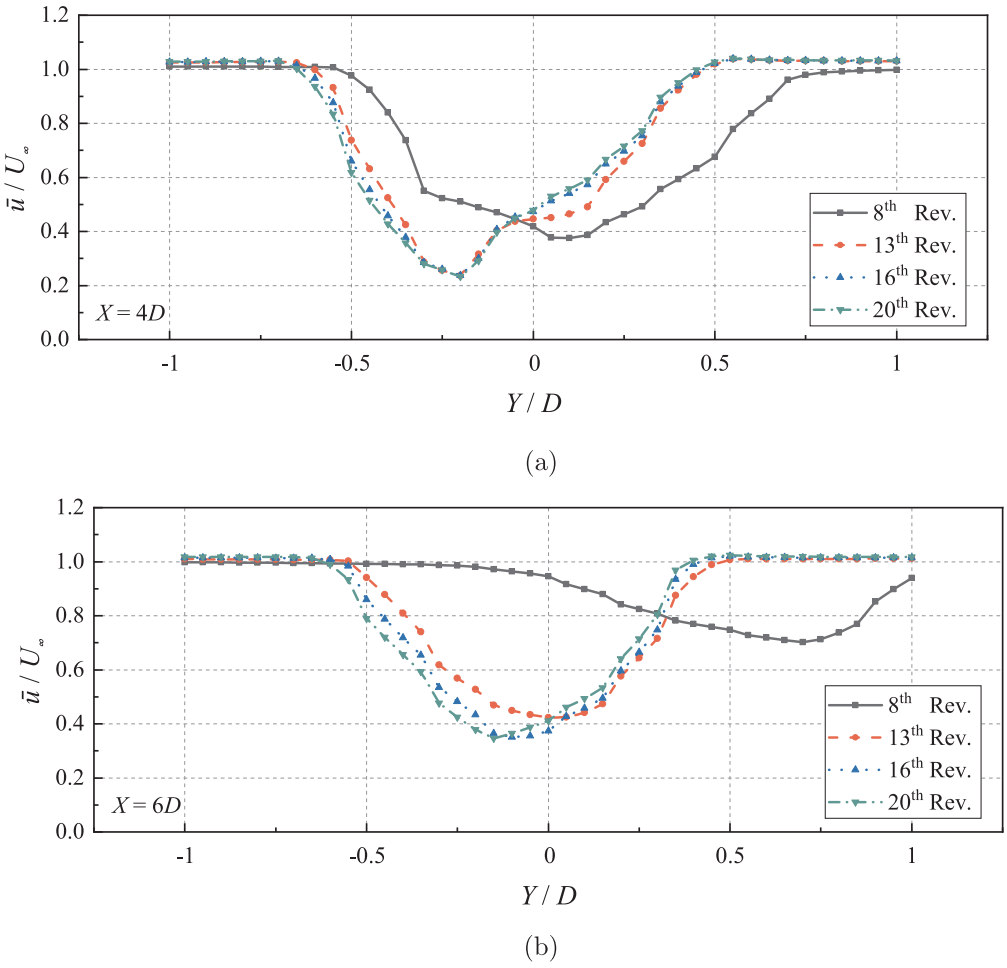

Fig. 20. Streamwise velocity distribution of the wind turbine wake at different distances with different revolutions: (a) $\Delta V = 0.6c$, $X = 4D$; (b) $\Delta V = 0.6c$, $X = 6D$.

wind turbine wake over the last revolution are shown in Fig. 21. The normalized streamwise wind velocity along the lateral lines (cross-wind direction) with different distances from the center of the rotor can be found in Fig. 21(b) and (c). The asymmetric distribution of streamwise velocity can be found in the wake both for the straight blade and V-shaped blade. And it can be clearly seen that as the wake develops, this asymmetry become more obvious at distance of $X = 6D$ compared to that of near field which is consistent with the findings in experiment [70]. Besides, the wind velocity deficit in the wake is evident for the straight blade at medium distance of $X = 5D$, which was confirmed as wake self-induction effect in the test [71]. Compared to that, the V-shaped blade has made great difference in the streamwise velocity distribution. On the mid span plane, the asymmetry of streamwise velocity distribution of the VAWT with V-shaped blade is opposite to that of the straight blade. Fig. 21(d) and (e) show the profiles of streamwise velocity on several lateral lines along the Z axis at distance of $X = 3D$. It is found that all low speed regions of the wake for the VAWT with straight blade move to the same side ($Y/D > 0$), while velocity deficit regions of the wake of V-shaped blade gradually move to the other side along the Z axis as shown in Fig. 21(e).

5. Conclusions

The present study investigated the aerodynamic performance of a novel VAWT with V-shaped blades. The SST $k - \omega$ model has been utilized to evaluate the effects of different V-shaped blades on the aerodynamic behaviors. The results indicate that the V-shaped blade has better performance in wind energy conversion compared to the baseline model.

The main conclusions are summarized as follows:

(1) Both the V-shaped blade and the inverted V-shaped blade can improve the performance of VAWT. The optimal power output can be found in the V-shaped blade with $\Delta V = 0.6c$, and the enhancement in power coefficient is more than 20%.
(2) The major positive contributions to the power output is generated within the region $30° \leqslant \theta \leq 150°$ and $180° \leqslant \theta \leq 340°$. And the reduction in the torque fluctuations of VAWT results in more stable performance and less rotor vibrations.
(3) The optimal V-shaped blade significantly reduces the drag coefficient in the region form $\theta = 120°$ to $\theta = 205°$. In this way, a higher lift-drag ratio compared to that of the straight blade is achieved.
(4) The V-shaped blade has a small effect on the thrust coefficient of VAWT, but effectively reduces the average lateral loads on the wind turbine.
(5) The straight blade suffers more severe dynamic stall compared with the V-shaped blade due to the irregular and complex cross-flow structures on the surface of the former one.
(6) The enhancement in power coefficient mainly attributes to the middle part of the V-shaped blade, while more energy is lost in the blade tip region. However, the blade tip effect of the V-shaped blade is not more severe than that of the straight blade.
(7) The utilization of V-shaped blade changes the distribution of local low speed region in the turbine wake, which should be taken into consideration in the wind farm scenario.

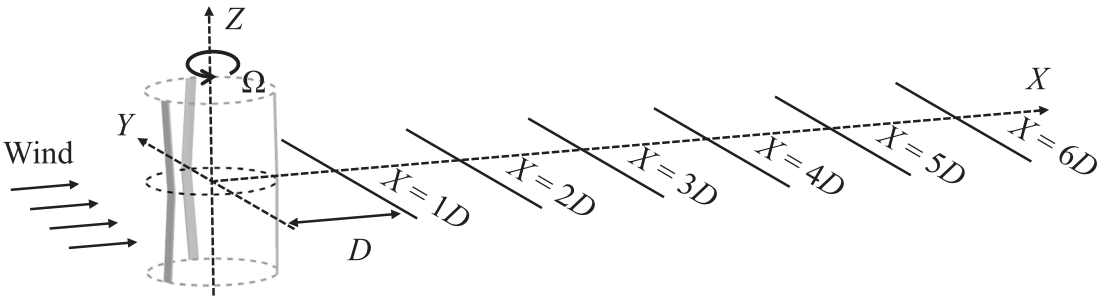

(a)

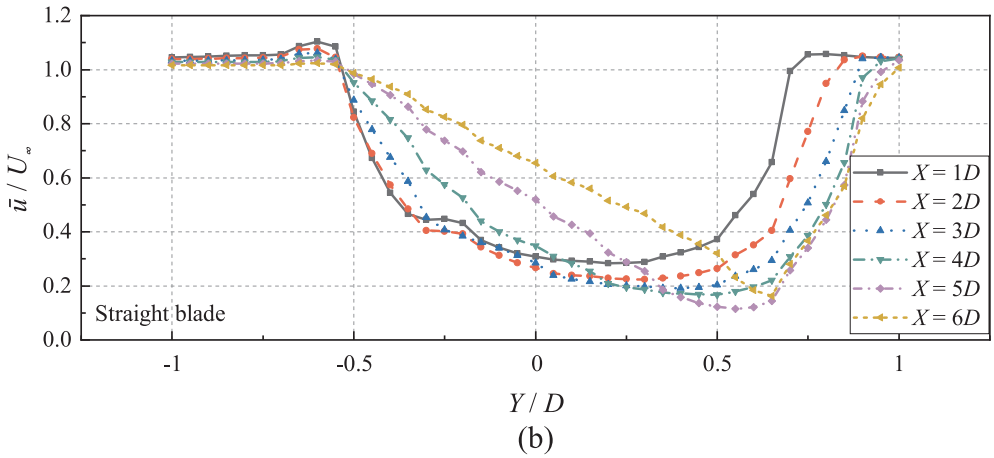

(b)

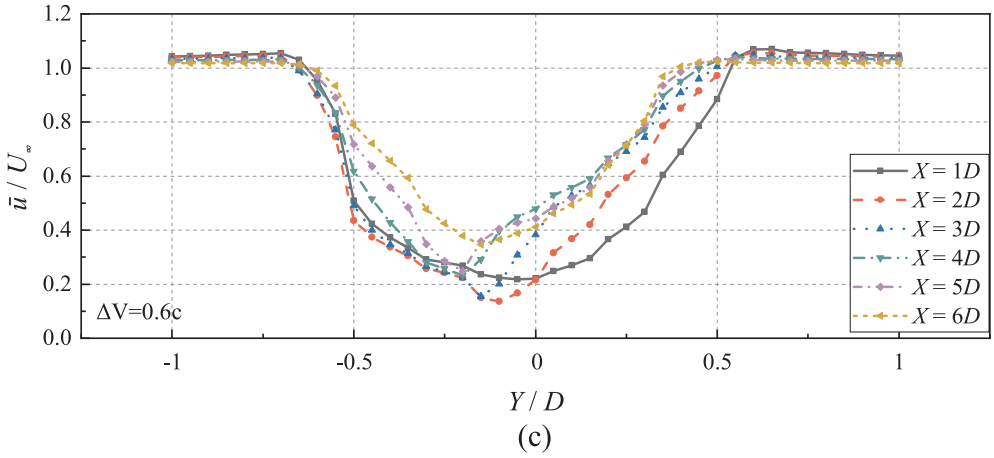

(c)

Fig. 21. Time-averaged streamwise velocity distribution of the wind turbine wake over the last revolution: (a) location of measuring points; (b) straight blade, $Z = 0$; (c) $\Delta V = 0.6c$, $Z = 0$; (d) straight blade, $X = 3D$; (e) $\Delta V = 0.6c$, $X = 3D$.

Overall, the results of the current work provide a new idea for improving the performance of VAWT. The V-shaped blade can be applied as an effective and potential solution for dynamic stall in wind turbines.

Declaration of Competing Interest

The authors declare that they have no known competing financial interests or personal relationships that could have appeared to influence the work reported in this paper.

Acknowledgments

The financial supports from the National Natural Science Foundation of China (Nos. 51879160, 51809170, 11772193 and 51679139), Innovation Program of Shanghai Municipal Education Commission (No. 2019-01-07-00-02-E00066), Project of Thousand Youth Talents, Program for Professor of Special Appointment (Eastern Scholar) at Shanghai Institutions of Higher Learning (Nos. ZXDF010037, ZXDF010040) are gratefully acknowledged. This research is also sponsored in part by Program for Intergovernmental International S&T Cooperation Projects of Shanghai Municipality (Nos. 18290710600, 19160713600), Program for International Cooperation of Shanghai Science and Technology (No. 18160744000), State Key Laboratory of Ocean Engineering (No. GKZD010075), and New Enrolment Support of Shanghai Jiao Tong University (No. WF220401005).

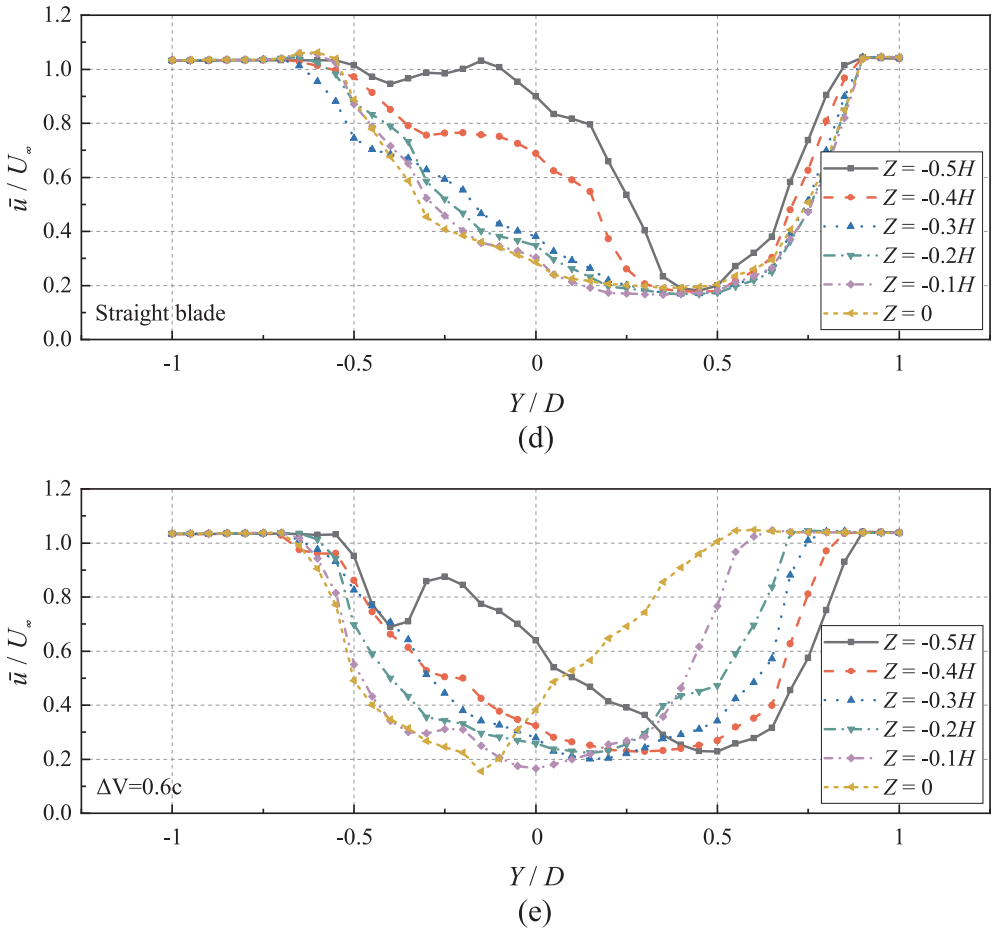

Fig. 21. (*continued*)

References

[1] Evans A, Strezov V, Evans TJ. Assessment of sustainability indicators for renewable energy technologies. Renew Sustain Energy Rev 2009;13:1082–8.

[2] Chehouri A, Younes R, Ilinca A, Perron J. Review of performance optimization techniques applied to wind turbines. Appl Energy 2015;142:361–88.

[3] Grujicic M, Arakere G, Pandurangan B, Sellappan V, Vallejo A, Ozen M. Multidisciplinary design optimization for glass-fiber epoxy-matrix composite 5 mw horizontal-axis wind-turbine blades. J Mater Eng Perform 2010;19:1116–27.

[4] Tjiu W, Marnoto T, Mat S, Ruslan MH, Sopian K. Darrieus vertical axis wind turbine for power generation ii: challenges in hawt and the opportunity of multi-megawatt darrieus vawt development. Renew Energy 2015;75:560–71.

[5] Balduzzi F, Bianchini A, Carnevale EA, Ferrari L, Magnani S. Feasibility analysis of a darrieus vertical-axis wind turbine installation in the rooftop of a building. Appl Energy 2012;97:921–9.

[6] Danao LA, Edwards J, Eboibi O, Howell R. A numerical investigation into the influence of unsteady wind on the performance and aerodynamics of a vertical axis wind turbine. Appl Energy 2014;116:111–24.

[7] Borg M, Collu M. Frequency-domain characteristics of aerodynamic loads of offshore floating vertical axis wind turbines. Appl Energy 2015;155:629–36.

[8] Paraschivoiu I. Double-multiple streamtube model for studying vertical-axis wind turbines. J Propul Power 1988;4:370–7.

[9] Soraghan CE, Leithead WE, Feuchtwang J, Yue H. Double multiple streamtube model for variable pitch vertical axis wind turbines. In: 31st AIAA applied aerodynamics conference, 2802.

[10] Bedon G, Paulsen US, Madsen HA, Belloni F, Castelli MR, Benini E. Computational assessment of the deepwind aerodynamic performance with different blade and airfoil configurations. Appl Energy 2017;185:1100–8.

[11] Wang L, Zhang L, Zeng N. A potential flow 2-d vortex panel model: applications to vertical axis straight blade tidal turbine. Energy Convers Manage 2007;48:454–61.

[12] Wang L, Yeung RW. On the performance of a micro-scale bach-type turbine as predicted by discrete-vortex simulations. Appl Energy 2016;183:823–36.

[13] Mandal A, Burton J. The effects of dynamic stall and flow curvature on the aerodynamics of darrieus turbines applying the cascade model. Wind Eng 1994:267–82.

[14] Rainbird JM, Bianchini A, Balduzzi F, Peiró J, Graham JMR, Ferrara G, et al. On the influence of virtual camber effect on airfoil polars for use in simulations of darrieus wind turbines. Energy Convers Manage 2015;106:373–84.

[15] Franchina N, Persico G, Savini M. 2d–3d computations of a vertical axis wind turbine flow field: Modeling issues and physical interpretations. Renew Energy 2019;136:1170–89.

[16] Lei H, Su J, Bao Y, Chen Y, Han Z, Zhou D. Investigation of wake characteristics for the offshore floating vertical axis wind turbines in pitch and surge motions of platforms. Energy 2019;166:471–89.

[17] Rezaeiha A, Kalkman I, Blocken B. Effect of pitch angle on power performance and aerodynamics of a vertical axis wind turbine. Appl Energy 2017;197:132–50.

[18] Ghasemian M, Ashrafi ZN, Sedaghat A. A review on computational fluid dynamic simulation techniques for darrieus vertical axis wind turbines. Energy Convers Manage 2017;149:87–100.

[19] Castelli MR, Ardizzon G, Battisti L, Benini E, Pavesi G, Modeling strategy and numerical validation for a darrieus vertical axis micro-wind turbine. In: ASME 2010 international mechanical engineering congress and exposition, Citeseer. p. 409–18.

[20] Battisti L, Persico G, Dossena V, Paradiso B, Castelli MR, Brighenti A, et al. Experimental benchmark data for h-shaped and troposkien vawt architectures. Renew Energy 2018;125:425–44.

[21] Mazarbhuiya HMSM, Biswas A, Sharma KK. Performance investigations of modified asymmetric blade h-darrieus vawt rotors. J Renew Sustain Energy 2018;10:033302.

[22] Li Q, Maeda T, Kamada Y, Murata J, Yamamoto M, Ogasawara T, et al. Study on power performance for straight-bladed vertical axis wind turbine by field and wind tunnel test. Renew Energy 2016;90:291–300.

[23] Miller MA, Duvvuri S, Brownstein I, Lee M, Dabiri JO, Hultmark M. Vertical-axis wind turbine experiments at full dynamic similarity. J Fluid Mech 2018;844:707–20.

[24] Xu YL, Peng YX, Zhan S. Optimal blade pitch function and control device for high-solidity straight-bladed vertical axis wind turbines. Appl Energy 2019;242:1613–25.

[25] Bausas MD, Danao LAM. The aerodynamics of a camber-bladed vertical axis wind turbine in unsteady wind. Energy 2015;93:1155–64.

[26] Chen J, Chen L, Xu H, Yang H, Ye C, Liu D. Performance improvement of a vertical axis wind turbine by comprehensive assessment of an airfoil family. Energy 2016;114:318–31.

[27] Subramanian A, Yogesh SA, Sivanandan H, Giri A, Vasudevan M, Mugundhan V, et al. Effect of airfoil and solidity on performance of small scale vertical axis wind turbine using three dimensional cfd model. Energy 2017;133:179–90.

[28] Li Q, Maeda T, Kamada Y, Shimizu K, Ogasawara T, Nakai A, et al. Effect of rotor aspect ratio and solidity on a straight-bladed vertical axis wind turbine in three-dimensional analysis by the panel method. Energy 2017;121:1–9.

[29] Ashwindran S, Aziz AA, Oumer A. Unsteady computational study of novel biologically inspired offshore vertical axis wind turbine at different tip speed ratios: A

two-dimensional study. Int J Automotive Mech Eng 2019;16:6753–72.
[30] Hand B, Kelly G, Cashman A. Numerical simulation of a vertical axis wind turbine airfoil experiencing dynamic stall at high reynolds numbers. Comput Fluids 2017;149:12–30.
[31] Peng H, Lam H. Turbulence effects on the wake characteristics and aerodynamic performance of a straight-bladed vertical axis wind turbine by wind tunnel tests and large eddy simulations. Energy 2016;109:557–68.
[32] Su J, Lei H, Zhou D, Han Z, Bao Y, Zhu H, et al. Aerodynamic noise assessment for a vertical axis wind turbine using improved delayed detached eddy simulation. Renew Energy 2019;141:559–69.
[33] Danao LA, Eboibi O, Howell R. An experimental investigation into the influence of unsteady wind on the performance of a vertical axis wind turbine. Appl Energy 2013;107:403–11.
[34] Ferreira CJS, Van Bussel GJ, Van Kuik GA. Wind tunnel hotwire measurements, flow visualization and thrust measurement of a vawt in skew. J Sol Energy Eng 2006;128:487–97.
[35] Lee KY, Tsao SH, Tzeng CW, Lin HJ. Influence of the vertical wind and wind direction on the power output of a small vertical-axis wind turbine installed on the rooftop of a building. Appl Energy 2018;209:383–91.
[36] Xu Z, Feng YH, Zhao CY, Huo YL, Li S, Hu XJ, et al. Experimental and numerical investigation on aerodynamic performance of a novel disc-shaped wind rotor for the small-scale wind turbine. Energy Convers Manage 2018;175:173–91.
[37] Pérez-Torró R, Kim JW. A large-eddy simulation on a deep-stalled aerofoil with a wavy leading edge. J Fluid Mech 2017;813:23–52.
[38] Wang Z, Zhuang M. Leading-edge serrations for performance improvement on a vertical-axis wind turbine at low tip-speed-ratios. Appl Energy 2017;208:1184–97.
[39] Arpino F, Scungio M, Cortellessa G. Numerical performance assessment of an innovative darrieus-style vertical axis wind turbine with auxiliary straight blades. Energy Convers Manage 2018;171:769–77.
[40] Chong WT, Muzammil WK, Wong KH, Wang CT, Gwani M, Chu YJ, et al. Cross axis wind turbine: Pushing the limit of wind turbine technology with complementary design. Appl Energy 2017;207:78–95.
[41] Liu K, Yu M, Zhu W. Enhancing wind energy harvesting performance of vertical axis wind turbines with a new hybrid design: A fluid-structure interaction study. Renew Energy 2019;140:912–27.
[42] Govind B. Increasing the operational capability of a horizontal axis wind turbine by its integration with a vertical axis wind turbine. Appl Energy 2017;199:479–94.
[43] Gorlov AM, Unidirectional helical reaction turbine operable under reversible fluid flow for power systems [1995], uS Patent 5,451,137.
[44] Kirke B. Tests on ducted and bare helical and straight blade darrieus hydrokinetic turbines. Renew Energy 2011;36:3013–22.
[45] Yang B, Shu X. Hydrofoil optimization and experimental validation in helical vertical axis turbine for power generation from marine current. Ocean Eng 2012;42:35–46.
[46] Scheurich F, Brown RE. Modelling the aerodynamics of vertical-axis wind turbines in unsteady wind conditions. Wind Energy 2013;16:91–107.
[47] Cheng Q, Liu X, Ji HS, Kim KC, Yang B. Aerodynamic analysis of a helical vertical axis wind turbine. Energies 2017;10:575.
[48] Marten D, Lennie M, Pechlivanoglou G, Paschereit CO, Bianchini A, Ferrara G, et al. Benchmark of a novel aero-elastic simulation code for small scale vawt analysis. J Eng Gas Turbines Power 2019;141:041014.
[49] Zamani M, Maghrebi MJ, Varedi SR. Starting torque improvement using j-shaped straight-bladed darrieus vertical axis wind turbine by means of numerical simulation. Renew Energy 2016;95:109–26.
[50] Ismail MF, Vijayaraghavan K. The effects of aerofoil profile modification on a vertical axis wind turbine performance. Energy 2015;80:20–31.
[51] Sobhani E, Ghaffari M, Maghrebi MJ. Numerical investigation of dimple effects on darrieus vertical axis wind turbine. Energy 2017;133:231–41.
[52] Paraschivoiu I, Wind turbine design: with emphasis on Darrieus concept. Presses inter Polytechnique; 2002.
[53] Ferreira CS, Geurts B. Aerofoil optimization for vertical-axis wind turbines. Wind Energy 2015;18:1371–85.
[54] Sagharichi A, Zamani M, Ghasemi A. Effect of solidity on the performance of variable-pitch vertical axis wind turbine. Energy 2018;161:753–75.
[55] Lei H, Zhou D, Bao Y, Li Y, Han Z. Three-dimensional improved delayed detached eddy simulation of a two-bladed vertical axis wind turbine. Energy Convers Manage 2017;133:235–48.
[56] Castelli MR, Englaro A, Benini E. The darrieus wind turbine: Proposal for a new performance prediction model based on cfd. Energy 2011;36:4919–34.
[57] Rahromostaqim M, Posa A, Balaras E. Numerical investigation of the performance of pitching airfoils at high amplitudes. AIAA J 2016:2221–32.
[58] Sim ao Ferreira C, Scheurich F. Demonstrating that power and instantaneous loads are decoupled in a vertical-axis wind turbine. Wind Energy 2014;17:385–96.
[59] McLaren K, Tullis S, Ziada S. Measurement of high solidity vertical axis wind turbine aerodynamic loads under high vibration response conditions. J Fluids Struct 2012;32:12–26.
[60] Hansen M. Improved modal dynamics of wind turbines to avoid stall-induced vibrations. Wind Energy: Int J Prog Appl Wind Power Convers Technol 2003;6:179–95.
[61] Huo T, Tong L. Wind-induced response analysis of wind turbine tubular towers with consideration of rotating effect of blades. Adv Struct Eng 2019. 1369433219865815.
[62] Cheng Z, Madsen HA, Gao Z, Moan T. Effect of the number of blades on the dynamics of floating straight-bladed vertical axis wind turbines. Renew Energy 2017;101:1285–98.
[63] Gülsaçan B, Şencan G, Yavuz MM. Effect of thickness-to-chord ratio on flow structure of a low swept delta wing. AIAA J 2018;56:4657–68.
[64] Medina A, Rockwood M, Garmann DJ, Visbal MR, Ahmed A. On the characteristics of three-dimensional dynamic tip stall on a swept wing. AIAA Scitech 2019;Forum:2324.
[65] Lombard JEW, Moxey D, Sherwin SJ, Hoessler JF, Dhandapani S, Taylor MJ. Implicit large-eddy simulation of a wingtip vortex. AIAA J 2015;54:506–18.
[66] Narayan G, John B. Effect of winglets induced tip vortex structure on the performance of subsonic wings. Aerosp Sci Technol 2016;58:328–40.
[67] Anderson Jr JD, Fundamentals of aerodynamics. Tata McGraw-Hill Education; 2010.
[68] Miao W, Li C, Pavesi G, Yang J, Xie X. Investigation of wake characteristics of a yawed hawt and its impacts on the inline downstream wind turbine using unsteady cfd. J Wind Eng Ind Aerodyn 2017;168:60–71.
[69] Lam H, Peng H. Study of wake characteristics of a vertical axis wind turbine by two- and three-dimensional computational fluid dynamics simulations. Renew Energy 2016;90:386–98.
[70] Araya DB, Dabiri JO. A comparison of wake measurements in motor-driven and flow-driven turbine experiments. Exp Fluids 2015;56:150.
[71] Tescione G, Ragni D, He C, Ferreira CS, Van Bussel G. Near wake flow analysis of a vertical axis wind turbine by stereoscopic particle image velocimetry. Renew Energy 2014;70:47–61.